P-ISSN 0126-3188
E-ISSN 2443-3926

BRIN
BADAN RISET
DAN INOVASI NASIONAL

METALURGI

VOLUME 37 ISSUE 1, APRIL 2022

SCIENTIFIC JOURNAL ACCREDITATION NUMBER NO.3/E/KPT/2019

The Effect of Heat Treatment and Surface Anodization on Wear and Friction Coefficient of 2024 Aluminum Using Pin-on-Disk Method

Dynamic Plastic Deformation Induced by Repetitive Hammering on Cr-Mn Austenitic Stainless Steel

Grain Growth Kinetics of Austenitic Stainless Steel 316L and the Relations between Grain Sizes and Hardness under Isothermal Conditions

Effectiveness of the Separation of Magnesium and Lithium from Seawater with Sodium Silicate Precipitation Process

The Effect of Voltage and Time in Synthesis of Manganese Dioxide from Manganese Sulfate Precursor

National Research and Innovation Agency

Publisher :
National Research and Innovation Agency (BRIN)
Kawasan Puspiptek Serpong, Tangerang Selatan, Banten, Indonesia, 15314

E-mail: jurnalmetalurgi@mail.lipi.go.id

Science and technology magazine, regularly published every year; one volume consists of 3 editions

METALURGI

VOLUME 37 NUMBER 1, APRIL 2022

P-ISSN 0126-3188
E-ISSN 2443-3926

ACCREDITATION : SK No. 3/E/KPT/2019

Preface..iii
Abstract..v

The Effect of Heat Treatment and Surface Anodization on Wear and Friction Coefficient of 2024 Aluminum using Pin-on-Disk Method

Tiya Khairina Izzati, et. al...................................1-6

Dynamic Plastic Deformation Induced by Repetitive Hammering on Cr-Mn Austenitic Stainless Steel

Syahwira Taqwa Triadi, et. al…………...............7-14

Grain Growth Kinetics of Austenitic Stainless Steel 316L and the Relations between Grain Sizes and Hardness under Isothermal Conditions

Moch Syaiful Anwar, et. al...............................15-20

Effectiveness of the Separation of Magnesium and Lithium from Seawater with Sodium Silicate Precipitation Process

Eko Sulistiyono, et. al......................................21-30

The Effect of Voltage and Time in Synthesis of Manganese Dioxide from Manganese Sulfate Precursor

Eka Fitri Wulandari, et. al...............................31-38

Index

PREFACE

Thanks to Allah SWT, because of the help of Allah Metalurgi Magazine, Volume 37 Number 1, April 2022, could present five articles.

The first article results from Tiya Khairina Izzati and colleagues' research activities on The Effect of Heat Treatment and Surface Anodization on Wear and Friction Coefficient of 2024 Aluminum Using Pin-on-Disk Method. Syahwira Taqwa Triadi presented the second article, Dynamic Plastic Deformation Induced by Repetitive Hammering on Cr-Mn Austenitic Stainless Steel. Moch Syaiful Anwar and his colleagues presented Grain Growth Kinetics of Austenitic Stainless Steel 316L and the Relations between Grain Sizes and Hardness under Isothermal Conditions in the following article. For the fourth article, Eko Sulistiyono and his colleagues discussed the Effectiveness of Magnesium and Lithium Separation from Seawater Using a Sodium Silicate Precipitation Process. The fifth article, written by Eka Fitri Wulandari and colleagues, discussed The Effect of Voltage and Time in the Synthesis of Manganese Dioxide from Manganese Sulfate Precursor.

Hopefully, the publication of this volume of Metalurgi Magazine will benefit the advancement of research in Indonesia.

EDITORIAL

METALURGI

ISSN 0126 – 3188 Vol. 37 No. 1 April 2022

Keywords sourced from articles. This abstract is reproduced without permission or fee.

UDC (OXDCF) 621.402

Tiya Khairina Izzati[a,] , Aristo Nugraha Putra[a], Budi Hartono Setiamarga[b], Yorina Sarah Francoise Lantang[b]* ([a]Material Science and Engineering Program Study, [b] Material Science and Engineering Research Group, Faculty of Mechanical and Aerospace Engineering, Bandung Institute of Technology)

Metalurgi, Vol. 37 No. 1 April 2022

The Effect of Heat Treatment and Surface Anodication on Wear and Friction Coefficient of 2024 Aluminum Using Pin-on-disk Method

The use of aluminum alloys as a material for engineering components that rub against each other is increasing, so it is important to know the friction characteristics of these aluminum alloys. In this study, 2024 aluminum was given heat treatment with variations in aging time or an anodization process. Then, the wear and friction coefficient tests were carried out using a pin tool on the disc. The effect of aging time and surface anodization on wear tests are carried out to determine the amount of wear, and the coefficient of friction test is carried out to determine the coefficient of friction of the material when it rubs against a pin made of AISI 52100 steel. The coefficient of friction test is carried out by adding lubrication type as a parameter. The test results showed that the aluminum alloy given heat treatment had better resistance than that not heat treated. This is because the heat treatment creates precipitates that can increase aluminum's hardness and wear resistance. Whereas for anodized aluminum alloy, the alumina layer can act as an abrasive grain when continuously given a high enough friction and load. Hence the wear testing mode changes from dry sliding wear to three-body abrasive wear and decreased wear resistance. From the friction coefficient test results, the aging time affects the hardness of the aluminum alloy, which leads to the value of the coefficient of friction. The harder the aluminum alloy surface, the smaller the coefficient of friction obtained. Furthermore, applying lubricant to the aluminum alloy will also decrease the value of the friction coefficient of the alloy. Lubricating oil will provide a more significant reduction in friction coefficient than air. Finally, the anodizing surface on the aluminum alloy will act as a lubricant reservoir when it occurs.

Keywords: 2024 Aluminum, wear resistance, coefficient of friction, pin-on-disk test

METALURGI

ISSN 0126 – 3188 Vol. 37 No. 1 April 2022

Keywords sourced from articles. This abstract is reproduced without permission or fee.

UDC (OXDCF) 620.112

Syahwira Taqwa Triadi[a], Cherly Selindiana[a], Hermawan Judawisastra[b], Aditianto Ramelan[b] ([a]Material Science and Engineering Program Study, [b] Material Science and Engineering Research Group, Faculty of Mechanical and Aerospace Engineering, Bandung Institute of Technology)

Metalurgi, Vol. 37 No. 1 April 2022

Dynamic Plastic Deformation Induced by Repetitive Hammering on Cr-Mn Austenitic Stainless Steel

Austenitic stainless steels have advantages, such as high ductility and good corrosion resistance. The cold working process can increase the hardness and strength of the material. However, because a metastable austenite phase occurs in that material, there is a phase change of γ austenite to α'-martensite and ε-martensite, which will reduce the ductility and its corrosion resistance. The strengthening process with DPD (dynamic plastic deformation) can prevent the formation of martensitic phases through repeated impact at high strain rates. This study analyzed microstructures and hardness evaluation on Cr-Mn austenitic stainless steel due to dynamic plastic deformation through the repetitive hammering method. Repetitive hammering with a strain rate of 6,2 s^{-1} on Cr-Mn austenitic stainless steels was carried out on five specimens with variations in the impact of 50, 100, 150, 250, and 350 times with impact energy of 486 J/cm^2; 2.207 J/cm^2; 2.569 J/cm^2; 6.070 J/cm^2; and 11.330 J/cm^2 respectively. Microstructure, hardness, and XRD (x-ray diffraction) analyses were carried out on Cr-Mn austenitic stainless steels before and after repetitive hammering. Metallography was carried out to observe the microstructure using an optical microscope. The hardness was tested through the Rockwell A hardness test. XRD examination was used to identify the phases formed and indications of nano-twins. The repetitive hammering process up to 350 times has succeeded in increasing hardness from 53.5 HRA to 71.6 HRA. Plastic deformation introduced by repetitive hammering produced slip bands, cross bands, wavy bands, and an indication of nano-twins formation and increased hardness.

Keywords: DPD (dynamic plastic deformation), repetitive hammering, nano-twins, Cr-Mn austenitic stainless steel, SFE (stacking fault energy))

METALURGI

ISSN 0126 – 3188 Vol. 37 No. 1 April 2022

Keywords sourced from articles. This abstract is reproduced without permission or fee.

UDC (OXDCF) 620.112

Moch Syaiful Anwar[a, b]*, Mayang Gita Pradisti[a], Septian Adi Candra[b], Erie Martides[c], Efendi Mabruri[b], Eddy Sumarno Siradj[a] ([a]Metallurgical and Materials Engineering, University of Indonesia, [b]Research Center for Metallurgy, National Research and Innovation Agency, [c]Research Center for Electric Power and Mechatronics, National Research and Innovation Agency)

Metalurgi, Vol. 37 No. 1 April 2022

Grain Growth Kinetics of Austenitic Stainless Steel 316L and the Relations Between Grain Sizes and Hardness under Isothermal Conditions

The 316L austenitic stainless steel is usually used in nuclear power plant. This steel has an austenitic phase at room temperature, and it can change grain size after being exposed at high temperatures. This study aims to investigate grain growth behavior and hardness of 316L austenitic stainless steel after cold-rolled and annealing to 1100 °C with holding times of 0, 900, 1800, 2700, 3600 s. The result showed that the grain growth of 316L austenitic stainless steel usually occurs. Austenite grain size of 316L increased with increasing holding time, resulting in hardness decreases. Experimental grain growth of 316L austenitic stainless steel shows no significant difference from the prediction, with an error of about 0.7. The highest Micro Vickers hardness is found at a grain size of 14.93 µm.

Keywords: Austenitic stainless steel 316L, grain growth kinetics, hardness, modeling

METALURGI

ISSN 0126 – 3188 Vol. 37 No. 1 April 2022

Keywords sourced from articles. This abstract is reproduced without permission or fee.

UDC (OXDCF) 546.38

Eko Sulistiyono[a], Sri Harjanto[a], Latifa Hanum Lalasari[b], Florentinus Firdiyono[b], Nadia Chrisayu Natasha[b], Yosephin Dewayani[b] ([a]Departments of Metallurgical and Materials Engineering, University of Indonesia, [b] Research Center for Metallurgy, National Research and Innovation Agency)

Metalurgi, Vol. 37 No. 1 April 2022

Effectiveness of the Separation of Magnesium and Lithium from Seawater with Sodium Silicate Precipitation Process

The purpose of this experiment was to separate magnesium ions and lithium ions from seawater in order to obtain a lithium concentrate solution product free of magnesium using a sodium silicate precipitation process. The sample used in this experiment was seawater from the Ancol Lagoon Area in North Jakarta. The seawater used has a high Mg/Li ratio of 10521 and contains 0.1674 ppm lithium ions and 1761 ppm magnesium ions. Before initial processing, seawater with high magnesium levels is not suitable as a raw material for the manufacture of lithium carbonate (active battery ingredient). The variables in the study were the addition of sodium silicate solution in amounts corresponding to 13, 27, 40, 53, 67, 80, 93, and 107% stoichiometry of magnesium ion. One step and multiple stages were used to add sodium silicate solution. The experimental results show that the addition of sodium silicate with 80% stoichiometry is the most effective, as indicated by a decrease in the Mg/Li ratio from 10521 to 64. The limitation of this study is that many lithium ions are still precipitated with magnesium silicate during the precipitation process, so the lithium ions lost in the filtrate reached 82.26% in the single-stage process. As a result, a multi-stage process with six processing steps was used. At single-stage optimum conditions, the sodium silicate addition was 1/6 of the volume of sodium silicate solution. The multi-stage process results could reduce lithium-ion loss in the filtrate from 82.26% to 76.54%. According to the findings of this study, the sodium silicate precipitation process was ineffective in separating lithium and magnesium ions from seawater in both single and multi-stage processes.

Keywords: Magnesium ion separation, lithium ion separation, sodium silicate residue, seawater

METALURGI

ISSN 0126 – 3188 Vol. 37 No. 1 April 2022

Keywords sourced from articles. This abstract is reproduced without permission or fee.

UDC (OXDCF) 546.54

Eka Fitri Wulandari[a], Lia Andriyah[b], Soesaptri Oediyani[a], Latifa Hanum Lalasari[b], Tri Arini[b], Nadia Crisayu Natasha[b], Fariza Eka Yunita[b], Ariyo Suharyanto[b], Eko Sulistiyono[b] ([a]Departemen Teknik Metalurgi, Sultan Ageng Tirtayasa University, [b]Research Center for Metallurgy, National Research and Innovation Agency)

Metalurgi, Vol. 37 No. 1 April 2022

The Effect of Voltage and Time in Synthesis of Manganese Dioxide from Manganese Sulfate Precursor

The utilization of manganese dioxide (MnO_2) as a cathode material for lithium-ion batteries has attracted considerable attention due to its high theoretical storage capacity of 615 mAh/g. In this study, the synthesis of MnO_2 was carried out from manganese sulfate ($MnSO_4$) precursor, a pregnant solution from the leaching process of manganese ore from Trenggalek Regency. The electrolysis method has been used in this synthesis of MnO_2 in an electrochemical cell consisting of two graphite electrodes with dimensions of (16 x 5 x 0.3) cm. The purpose of this study is to determine the effect of voltage and time on particles produced of MnO_2, the phase and crystal structure by MnO_2, and its morphological microstructure. The electrolysis process was carried out in 2,000 ml of $MnSO_4$ solution under constant stirring at 60 °C with DC voltage varied by 2, 4, 6, and 8 volt and time run by 4, 8, 12, and 16 hours. The precipitates formed at the anode were separated, then the particles were dried at 110°C for 2 hours. The composition of MnO_2 was analyzed by XRF (x-ray fluorescence), the phase and crystal structure were evaluated by XRD (x-ray diffraction), and the morphological microstructure was captured by SEM (scanning electron microscope). The results revealed that the highest mass gain of MnO_2 produced is 31.63 grams which are electrolyzed at 8 volts for 16 hours. The highest purity of MnO_2 is 89.23% which is electrolyzed at 2 volts for 16 hours. The particles produced were α-MnO_2 with a tetragonal crystal system and nearly spherical with size particles ranging from 136.01-202.48 and 144-352 nm.

Keywords: Manganese sulfate, manganese dioxide, electrolysis, crystal structure, polymorphy

METALURGI
Majalah Ilmu dan Teknologi
p-ISSN 0126-3188 | e-ISSN 2443-3926
ejurnalmaterialmetalurgi.lipi.go.id

THE EFFECT OF HEAT TREATMENT AND SURFACE ANODIZATION ON WEAR AND FRICTION COEFFICIENT OF 2024 ALUMINUM USING PIN-ON-DISK METHOD

Tiya Khairina Izzati[a], Aristo Nugraha Putra[a], Budi Hartono Setiamarga[b], Yorina Sarah Francoise Lantang[b]*
[a]Material Science and Engineering Program Study
[b] Material Science and Engineering Research Group
Faculty of Mechanical and Aerospace Engineering, Bandung Institute of Technology
Jl. Ganesha 10 Bandung, Indonesia 40132
*E-mail: yorina.lantang@itb.ac.id

Received : 23-12-2021, Revised : 11-05-2022, Accepted : 23-06-2022

Abstract

The use of aluminum alloys as a material for engineering components that rub against each other is increasing, so it is important to know the friction characteristics of these aluminum alloys. In this study, 2024 aluminum was given heat treatment with variations in aging time or an anodization process. Then, the wear and friction coefficient tests were carried out using a pin tool on the disc. The effect of aging time and surface anodization on wear tests are carried out to determine the amount of wear, and the coefficient of friction test is carried out to determine the coefficient of friction of the material when it rubs against a pin made of AISI 52100 steel. The coefficient of friction test is carried out by adding lubrication type as a parameter. The test results showed that the aluminum alloy given heat treatment had better resistance than that not heat treated. This is because the heat treatment creates precipitates that can increase aluminum's hardness and wear resistance. Whereas for anodized aluminum alloy, the alumina layer can act as an abrasive grain when continuously given a high enough friction and load. Hence the wear testing mode changes from dry sliding wear to three-body abrasive wear and decreased wear resistance. From the friction coefficient test results, the aging time affects the hardness of the aluminum alloy, which leads to the value of the coefficient of friction. The harder the aluminum alloy surface, the smaller the coefficient of friction obtained. Furthermore, applying lubricant to the aluminum alloy will also decrease the value of the friction coefficient of the alloy. Lubricating oil will provide a more significant reduction in friction coefficient than air. Finally, the anodizing surface on the aluminum alloy will act as a lubricant reservoir when it occurs.

Keywords: *Aluminum 2024, wear resistance, coefficient of friction, pin-on-disk test*

1. INTRODUCTION

Technological advancements in engineering components constantly need suiting material to function efficiently. Aluminum alloys are one of the most widespread base materials and have had an important role in the aerospace and automotive industry [1]. Aluminum has a lower density than ferrous metal's [2]. Furthermore, aluminum's melting point is much lower than that of ferrous metal. The low melting point lowers aluminium's the processing energy and costs, and its low density makes aluminum-based components lightweight [3].

The 2xxx series aluminum alloys are one of the most commonly used alloys in the industry. This series incorporates copper (Cu) and magnesium (Mg) as alloying metals to get new and better properties [4]. The presence of Cu and Mg provides higher strength for aluminum alloy due to the precipitation strengthening phenomenon [5]. Precipitation strengthening is one of the most common strengthening methods in aluminum alloys. Precipitation strengthening occurs when alloys are subjected to a specific heat treatment; the different heat treatment processes will yield different strengthening

DOI : 10.14203/metalurgi.v37i1.620

Metalurgi is Sinta 2 Journal (https://sinta.ristekbrin.go.id/journals/detail?id=3708) accredited by Ministry of Research & Technology, Republic of Indonesia

results. The presence of precipitate also increases the hardness of the material [6].

Furthermore, increasing the hardness of aluminum alloys can also be done by surface treatment such as anodization. Anodization creates an oxide layer on the surface that will increase the hardness of the aluminum surface [7]. The oxide layer formation has been proven effective in tribological applications, as it can act as a reservoir for lubricants, thus increasing the friction and wearability of the component [8].

The increase of hardness in aluminum alloys, heat treatment and anodizing provides the alloys with better wearability [9]. This is why aluminum alloys are commonly used in applications such as cylinder block components and piston insert rings, which require good tribological properties [10]. Wearability is a very critical property in tribological applications. By thoroughly engineering wearability, it is estimated that one can save 1,6% of GDP, which equals more than 100 billion USD yearly in the United States [11]. Nevertheless, material choice is not the only variable determining wearability. Velocity and load are also important variables of wearability [12].

Moreover, two surfaces that rub against each other produce frictional force, which is determined by the friction coefficient. Frictional forces are sometimes wanted in one application but need to be minimalized in another. Thus, it is important to decide on the alloy's friction coefficient value so that it can be well-suited according to the application demands. Therefore, research needs to be conducted to determine these coefficient values.

This research observes the effect of the aging time and anodization on the wearability and friction coefficient. The tests are conducted with the pin-on-disk method.

2. MATERIALS AND METHODS

2.1 Materials

The aluminum alloy used in this research was 2024 aluminum (2024 Al) plate provided by PT GMF Aero Asia. Table 1 shows the chemical composition of 2024 Al. The 2024 Al sample used was in the form of a 65×65×2 mm plate. The sample plate was subjected to heat treatment or anodization before being tested for wearability and friction coefficient. There are five samples of 2024 Al, each subjected to different treatments. The first sample was not subjected to any treatment, coded T0. The samples coded T3, T6, and T9 were subjected to various heat treatment processes.

Table 1. Chemical composition of 2024 aluminum

Element	% Weight
Al	97.508
Cr	0.003
Cu	1.394
Fe	0.221
Mg	0.531
Mn	0.160
Si	0.097
Ti	0.025
Zn	0.042
Ni	0.005
Sn	0.003
Sb	0.008

The sample TA was subjected to anodization.

2.2 Sample Preparation

The sample used in this experiment was in the form of a 65×65×2 mm plate. To accommodate the shape and dimension of the samples in order to be fit in the pin-on-disk test equipment, the sample was cut into 20×20×2 mm.

Figure 1. Sample being held by a 3D printed sample holder

Next, the sample holder was made using a 3D printer from PLA material. The sample was fixated on the sample holder using an M2 bolt and ring, as shown in Fig. 1.

2.3 Heat Treatment and Anodization

In the heat treatment, heating was done to form supersaturated solid solution, followed by artificial aging. Both processes were done using SAKAE electrical furnace provided by PT GMF Aeroasia. There were three 2024 Al samples subjected to heat treatment with variation aging time. All three samples were heated at 490 ℃ for 35 minutes. After that, the samples were rapidly cooled to room temperature to form a supersaturated solid solution. Then, the samples were artificially aged at 190 ℃ for 3 hours for T3, 6 hours for T6, and 9 hours for T9.

The TA sample was anodized in H_2CrO_4 solution for 55 minutes at 35 ºC. Then, the sample was sealed at 90 ºC for 28 minutes.

2.4 Hardness Test

The hardness test was conducted using the Mituyo Rockwell hardness testing machine, provided by PT GMF AeroAsia, at room temperature using a steel ball indentor (1/16 in) and 100 kgf load.

2.5 Wear Test

A wear test was performed using 540 grams of load and an average rotational speed of 1370-1400 rpm for 120 minutes.

Figure 2. Pin-on-disk wear test machine

The test machine used a 150Watt DC motor and was powered by AC electricity, thus creating fluctuation in rotational speed at 1370-1400 rpm range. Nonetheless, the deviation in test results was still relatively negligible. The wear test machine used was a pin-on-disk test machine designed by an undergraduate student of Materials Engineering, Institut Teknologi Bandung, as shown in Fig. 2. The pin used in the test was 5 mm in diameter, made from AISI 52100 steel ball.

Sample mass loss was used to calculate sample wear. The greater the mass loss, the greater the wear. As a result, sample weighing must be done with care.

2.6 Coefficient of Friction Test

In this experiment, the coefficient of friction was determined from the friction test using the previous pin-on-disk test machine.

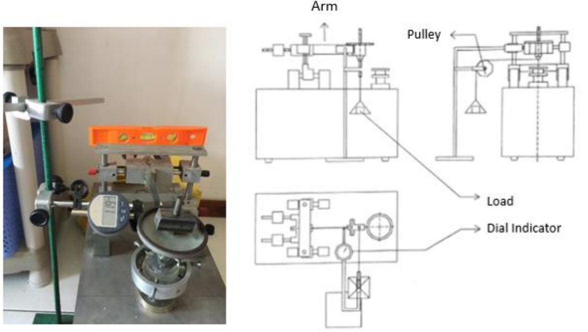

Figure 3. Coefficient of friction test tool

Calibration was carried out as an empirical approach to this friction test. The purpose of this step was to obtain valid data from the friction test. In this test, the frictional force between the sample and the pin will cause a deflection in the arm (Fig. 3). The amount of deflection was then converted into the coefficient of friction. In the tool calibration process, the frictional force will be replaced by the weight of the load, which will cause deflection. Several additional tools were needed to support the calibration process, such as pulleys, steel wires, wire clamps, load containers, level indicators, dial indicators, and loads with varied values (the load is weighed, and the time is recorded). Then, the tool was prepared according to the scheme in Fig. 3.

This research was carried out with a fixed load of 100 grams with variations in lubricant: water lubricant, oil lubricant, and without lubricant. The lubricant oil used in this test was AHM Oil MPX 2 (SAE 10W-30) engine oil. Before testing, all samples except the anodized sample were sanded with 800 grit sandpaper to uniform the surface roughness of the samples. The anodized sample was not sanded because the sanding process would remove the anodized layer formed on the sample surface.

3. RESULT AND DISCUSSION

Figure 4 shows that after three hours of aging, the hardness value of 2024 Al increased to 60.3 HRB. The hardness value, however, decreased with increasing aging time of 6 and 9 hours. Over aging occurs when aging is performed for between 6 and 9 hours.

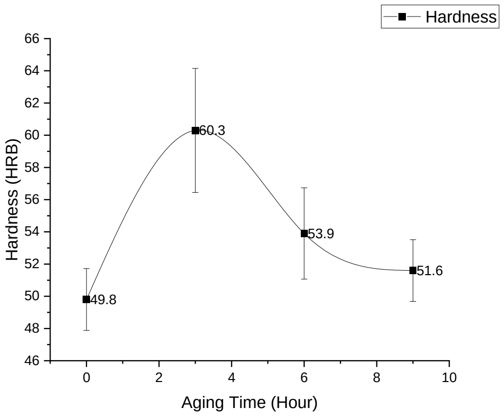

Figure 4. The hardness value (HRB) of 2024 Al with various aging time

The increase in hardness when the aging time was carried out for 3 hours was due to the strengthening of the precipitate, which hindered the dislocation motion. At this maximum hardness value, the precipitate is in a semi-coherent phase. This semi-coherent arrangement of atoms will produce a significant lattice distortion, so a greater force is needed for the dislocations to move through the existing strain field. If aging is left longer, for example, 6 hours and 9 hours, the precipitate atoms will have time to arrange themselves into a more stable phase, namely the incoherent phase. In this phase, the lattice distortion is reduced so the strain field that arises is smaller. This phenomenon will cause decreasing the hardness value. This finding is also in line with the study [14], where the hardness will increase until it reaches a maximum and then decrease if we hold the aging process longer.

3.1 Wear Test Results

The wear test in this study was carried out by providing a load of 540 grams. The average rotational speed was in the range of 1370-1400 rpm for 120 minutes. The wear test uses a 150-watt DC dynamo.

Figure 5 shows that the anodized material has the greatest mass loss. Several things can cause this; first, the oxide layer formed is not optimal, so this layer is easily damaged when subjected to continuous friction. The cause of the non-optimal layer formation is the high anodization temperature so that the pores formed are large and coarse, and the structure of the oxide layer formed is random [13]. The second point, using an indenter as a ball, causes the pressure on the surface to be significant. The sliding motion makes the easily damaged oxide layer more easily lost and eroded. The damaged oxide layer can become wear debris and then become abrasive. The wear debris is between the pins, forming a three-body abrasive wear mechanism [13]-[14].

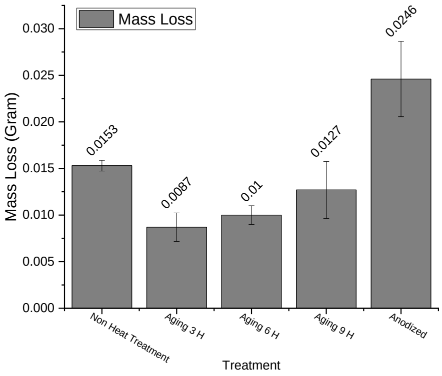

Figure 5. Average mass loss of 2024 Al with various treatments

The last point is that a continuous oscillating load on the same path supported by abrasive materials can create fatigue wear which causes micro-cracks on the surface so more material wears out. According to research [8], where the hard alumina layer becomes wear debris, it can cause micro-cracks so that wear occurs more quickly, as in [14], where the abrasive wear mechanism also occurs.It can be seen in Fig. 6 that the wear value is inversely proportional to the hardness value of the heat-treated 2024 Al.

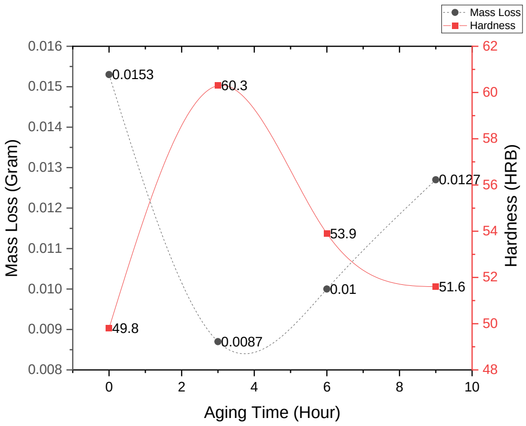

Figure 6. Effect of hardness value on mass loss in heat treated 2024 Al

The material with the highest hardness value will have the lowest wear value. According to the study [15], the heat-treated 2024 Al will increase their wear resistance and are directly proportional to their hardness.

3.2 Friction Coefficient Test Results

As explained in section 2.6, the pin-on-disk coefficient of friction test tool is calibrated before testing the coefficient of friction. Varied masses are weighed and converted to weight, and the resulting deflection values are recorded. The calibration process results will be plotted into a graph, and linear regression is performed on the calibration curve to obtain the calibration equation.

By using linear regression, the linear equation of the curve is obtained, namely:

$$F_{\text{friction}} = 0.2282x + 0.177 \tag{1}$$

Where x is the deflection in mm and F is friction in N. Then, the frictional force is converted to a coefficient of friction using the following equation.

$$\mu = \frac{F_{\text{friction}}}{N} \tag{2}$$

It can be seen in Fig. 7 that the 2024 Al with different aging times without using lubricants have different coefficients of friction. This shows that the aging time carried out on 2024 Al will affect the value of the coefficient of friction. As explained in the previous sub-chapter, the aging time on 2024 Al will affect its hardness value.

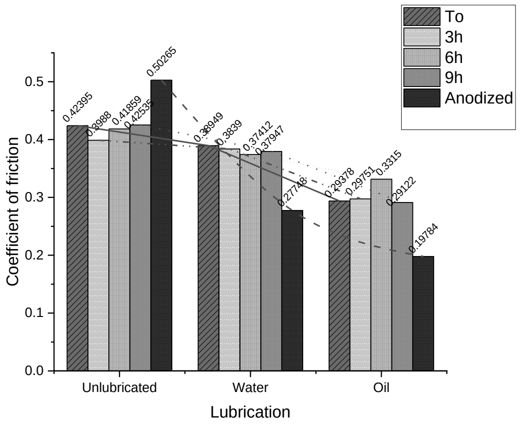

Figure 7. Graph of 2024 Al coefficeint of friction value

As shown in Fig. 8, the 2024 Al with an aging time of 3 hours has the highest hardness value and the lowest coefficient of friction. The harder the alloy surface, the smaller the coefficient of friction obtained, and vice versa. Material with lower hardness will make the penetration of the pin caused by normal forces deeper than the harder material.

Thus, in softer materials, the real contact area of the pin that rubs against the 2024 Al will be greater. When the contact area becomes wider, the adhesion force on the contact surface becomes greater, and it causes the friction that occurs will be even greater.

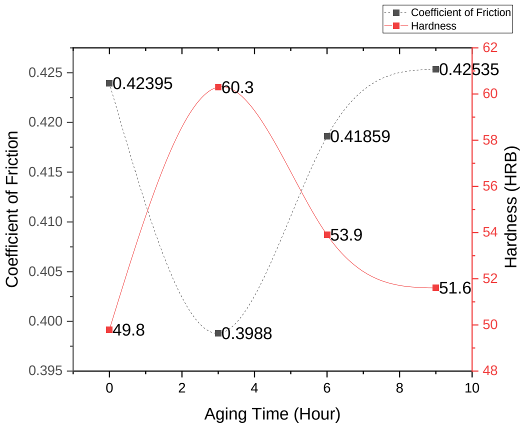

Figure 8. Hardness and coefficient of friction unlubricated 2024 Al curve

It can be seen in Fig. 7 that the coefficient of friction of the anodized 2024 Al has a different value than the other four samples. It means that the anodized surface will affect the coefficient of friction for 2024 Al. The coefficient of friction for the anodized 2024 Al is higher than the others. It is because the surface of the anodized is not polished. It is feared that this process can remove the anodizing layer that has formed. Thus, the surface roughness of the 2024 Al anodized will be different, and the coefficient of friction will be higher than the others. It can also be seen that the friction coefficient value of anodized 2024 Al lubricated during testing had a much lower coefficient of friction than the other four samples. It could be seen that applying lubricants could significantly reduce the coefficient of friction compared to the others. That happens because the presence of an anodized layer in the form of a pore can be a place for storing lubricants. Thus, the lubrication process at the contact of the two materials that takes will be better than in samples that do not have pores as a lubricant reservoir [14].

4. CONCLUSION

The wear resistance and coefficient of friction of 2024 Al are obtained by testing with the pin-on-disk tool. Heat treatment will affect the hardness value of 2024 Al. The highest hardness value of 2024 Al that have gone through the heat treatment process is achieved by giving aging treatment for 3 hours around 60.3 HRB. The 2024 Al with the highest hardness value has the best wear resistance value (lowest mass loss) and the lowest friction coefficient. The wear resistance and hardness are directly proportional. When the hardness increases, the wear resistance of 2024 Al will also increase. Furthermore, the friction coefficient of 2024 Al is inversely proportional to its hardness value; the harder the 2024 Al, the lower the friction coefficient value. Imperfect formation of the anodizing layer will cause the wear resistance to be lower.

The addition of lubricants can reduce the friction coefficient of 2024 Al. Lubricating oil will reduce the coefficient of friction more significantly than water lubricants. This is because the oil's viscosity is around 170 cP, while the viscosity of water at the same temperature is only about 1,0005 cP. Lubricants with higher viscosity will produce a thicker layer at the contact between the two surfaces. Therefore, the oil can create a thick layer on the contact surface so that the non-uniformity of the surface is not too influential when the friction occurs. The presence of a shaped oxidation layer will be useful as a lubricant reservoir so that the coefficient of friction of the anodized 2024 Al and added with lubricant will produce the smallest value.

ACKNOWLEDGMENT

The authors would like to express their gratitude to the PT GMF Aeroasia Tbk and Institut

Teknologi Bandung for their support and encouragement of this work.

REFERENCES

[1] M. S. Narassima, S. Ilangovan, S. P. Anbuudayasankar, and P. Pavithran, "Effect of reinforcement and aging time on wear behavior and mechanical properties of aluminum LM4," *Int. J. Eng. Adv. Technol.*, vol. 8, no. 5, pp. 2426-2433, 2019.

[2] M. Liang, L. Chen, G. Zhao, and Y. Guo, "Effects of solution treatment on the microstructure and mechanical properties of naturally aged EN AW 2024 Al alloy sheet," *J. Alloys Compd.*, vol. 824, pp. 153943, 2020. Doi: 10.1016/j.jallcom.2020.153943.

[3] George E Totten; D Scott McKenzie, *Handbook of Aluminum Volume 1 Physical Metallurgy and Process*. pp 416, New York: Marcel Dekker, 2003.

[4] J. R. Davis, *Aluminum and Aluminum Alloys*. pp 120, ohio: ASM International handbook, 2003.

[5] S. P. Shamchi, F. J. M. Queirós de Melo, P. J. Tavares, and P. M. G. P. Moreira, "Thermomechanical characterization of Alclad AA2024-T3 aluminum alloy using split Hopkinson tension bar," *Mech. Mater.*, vol. 139, , pp. 103198, 2019. Doi: 10.1016/j.mechmat.2019.103198.

[6] N. D. Alexopoulos, Z. Velonaki, C. I. Stergiou, and S. K. Kourkoulis, "Effect of ageing on precipitation kinetics, tensile and work hardening behavior of Al-Cu-Mg (2024) alloy," *Mater. Sci. Eng. A*, vol. 700, no. March, pp. 457-467, 2017. Doi: 10.1016/j.msea.2017.05.090.

[7] ASM, *ASM Handbook Volume 5 Surface Engineering*. pp.1416-1417, ASM International handbook, 1994.

[8] E. S. Spigarelli, C. Marcello, A. M. S. Hamouda, M. Farayi, and S. Anton Popelka, "Dry sliding tribological properties of a hard anodized AA6082 aluminum alloy," *Metals (Basel).*, vol. 10, no. 2, 2020. Doi: 10.3390/met10020207.

[9] ASM, *ASM Handbook Volume 18 Friction Lubrication and Wear Technology*. pp. 800-802, ASM International handbook, 1992.

[10] R. N. Rao and S. Das, "Wear coefficient and reliability of sliding wear test procedure for high strength aluminum alloy and composite," *Mater. Des.*, vol. 31, no. 7, pp. 3227-3233, 2010. Doi: 10.1016/j.matdes.2010.02.017.

[11] M. Gavgali, Y. Totik, and R. Sadeler, "The effects of artificial aging on wear properties of AA 6063 alloy," *Mater. Lett.*, vol. 57, no. 24-25, pp. 3713-3721, 2003. Doi: 10.1016/S0167-577X(03)00168-X.

[12] C. Y. H. Lim, S. C. Lim, and M. Gupta, "Wear behaviour of SiCp-reinforced magnesium matrix composites," *Wear*, vol. 255, no. 1-6, pp. 629-637, 2003. Doi: 10.1016/S0043-1648(03)00121-2.

[13] J. Lu, G. Wei, Y. Yu, C. Guo, and L. Jiang, "Aluminum alloy AA2024 anodized from the mixed acid system with enhanced mechanical properties," *Surfaces and Interfaces*, vol. 13, pp. 46-50, 2018. Doi: 10.1016/j.surfin.2018.08.003.

[14] G. S. Lee, J. H. Choi, Y. C. Choi, S. D. Bu, and Y. Z. Lee, "Tribological effects of pores on an anodized Al alloy surface as lubricant reservoir," *Curr. Appl. Phys.*, vol. 11, no. 5 SUPPL., pp. S182–S186, 2011. Doi: 10.1016/j.cap.2011.03.057.

[15] Ian Hutchings, *Tribology Friction and Wear of Engineering Materials Second Edition*. pp.106, Matthew Deans, 2006.

Metalurgi (2022) 1: 7 - 14

METALURGI
Majalah Ilmu dan Teknologi
p-ISSN 0126-3188 | e-ISSN 2443-3926
ejurnalmaterialmetalurgi.lipi.go.id

DYNAMIC PLASTIC DEFORMATION INDUCED BY REPETITIVE HAMMERING ON CR-MN AUSTENITIC STAINLESS STEEL

Syahwira Taqwa Triadi[a], Cherly Selindiana[a], Hermawan Judawisastra[b,*], Aditianto Ramelan[b]
[a] Material Science and Engineering Program Study
[b] Material Science and Engineering Research Group
Faculty of Mechanical and Aerospace Engineering, Bandung Institute of Technology
Jl. Ganesha 10 Bandung, Indonesia 40132
*E-mail: Hermawan.Judawisastra@material.itb.ac.id

Received : 22-12-2021, Revised : 15-04-2022, Accepted : 23-06-2022

Abstract

Austenitic stainless steels have advantages, such as high ductility and good corrosion resistance. The cold working process can increase the hardness and strength of the material. However, because a metastable austenite phase occurs in that material, there is a phase change of γ austenite to α'-martensite and ε-martensite, which will reduce the ductility and its corrosion resistance. The strengthening process with DPD (dynamic plastic deformation) can prevent the formation of martensitic phases through repeated impact at high strain rates. This study analyzed microstructures and hardness evaluation on Cr-Mn austenitic stainless steel due to dynamic plastic deformation through the repetitive hammering method. Repetitive hammering with a strain rate of 6,2 s^{-1} on Cr-Mn austenitic stainless steels was carried out on five specimens with variations in the impact of 50, 100, 150, 250, and 350 times with impact energy of 486 J/cm^2; 2.207 J/cm^2; 2.569 J/cm^2; 6.070 J/cm^2; and 11.330 J/cm^2 respectively. Microstructure, hardness, and XRD (x-ray diffraction) analyses were carried out on Cr-Mn austenitic stainless steels before and after repetitive hammering. Metallography was carried out to observe the microstructure using an optical microscope. The hardness was tested through the Rockwell A hardness test. XRD examination was used to identify the phases formed and indications of nano-twins. The repetitive hammering process up to 350 times has succeeded in increasing hardness from 53.5 HRA to 71.6 HRA. Plastic deformation introduced by repetitive hammering produced slip bands, cross bands, wavy bands, and an indication of nano-twins formation and increased hardness.

Keywords: *DPD (dynamic plastic deformation), repetitive hammering, nano-twins, Cr-Mn austenitic stainless steel, SFE (stacking fault energy)*

1. INTRODUCTION

Austenitic stainless steel is widely used due to its good corrosion resistance, formability, and weldability. However, austenitic stainless steel relatively has low mechanical properties compared to other types of steel (around 100-400 MPa) due to its FCC (face center cubic) structure [1]–[4]. To enhance its mechanical properties, cold working is commonly used on austenitic stainless steel to create high strength martensite phase. However, martensite formation on the austenitic stainless steel could reduce its corrosion resistance [5]-[6].

In the previous study carried out on the 316L austenitic stainless steel [7], a high strain rate is needed to prevent the formation of the martensite phase and maintain austenitic stainless steel with high ductility and good corrosion resistance [7]-[8]. With a high strain rate, the phenomenon is mechanical twinning with the formation of nano-twin grains in austenitic stainless steels [7], [9]. The volume fraction of the nano-twin is about 8% in austenitic stainless steels, increasing the yield strength of the material by more than 25% [11]. One method for forming nano-twin is dynamic plastic deformation (DPD) [7], [11]-[14].

The formation of the nano-twin will be influenced by the material's SFE (stacking fault energy) value. The mechanical twinning phenomenon will be activated if the stacking

DOI : 10.14203/metalurgi.v37i1.618

Metalurgi is Sinta 2 Journal (https://sinta.ristekbrin.go.id/journals/detail?id=3708) accredited by Ministry of Research & Technology, Republic of Indonesia

fault energy is between 20 to 50 mJ/m^2, below which martensite formation is more accessible [15]. In addition, austenitic stainless steel material has a metastable austenite phase that is easily transformed into martensite when cold working at temperatures farther away from Md_{30} [16]- [17]. Md_{30} is the temperature at which 50% martensite is formed after 30% true strain. Thus, as the temperature gets colder and closer to the Md_{30} temperature, the austenite is more stable and difficult to transform into α'-martensite or ε-martensite in austenitic stainless steels [16].

In this study, dynamic plastic deformation DPD was carried out using low-cost laboratory-made repetitive hammering, which has the working principle of repeatedly dropping the load on the specimen. Then we will study dynamic plastic deformation treatment through the repetitive hammering method on austenitic Cr-Mn stainless steel material with manganese as a substitute of nickel as an austenite former [18]. After the repetitive hammering process, its microstructure and hardness were analyzed to prove the strengthening mechanism of the Cr-Mn austenitic stainless steel through this treatment.

2. MATERIALS AND METHODS

2.1 Materials

Cr-Mn austenitic stainless steel with 10% Mn and 13% Cr was used in this study.

Table 1. Actual chemical composition of Cr-Mn austenitic stainless steel

Elements (wt%)							
C	**Si**	**S**	**P**	**Mn**	**Ni**	**Cr**	**Fe**
0.058	0.36	0.017	0.049	10.468	1.26	13.63	73.22

The specimen's chemical composition was characterized through OES (optical emission spectroscopy), as shown in Table 1.

2.2 Methods

The following equations (1) and (2) are used to calculate the value of SFE (stacking fault energy) [4], [8], [18], and Md_{30} temperature [16]-[17].

$$\text{SFE (mJ/m}^2\text{)} = 2{,}2 + 1{,}9\text{Ni} - 2{,}9\text{Si} + 0{,}77\text{Mo} + 0{,}5\text{Mn} + 40\text{C} - 0{,}016\text{Cr} - 3{,}6\text{N} \tag{1}$$

$$Md_{30}\text{, Angel} = 413 - 462\,(\text{C+N}) - 9.2\text{Si} - 8.1\text{Mn} - 13.7\text{Cr} - 9.5\text{Ni} - 18.5\text{Mo} \tag{2}$$

Solution annealing treatment was conducted to eliminate the deformation process on the as-received specimen at 1050 °C for 2 hours [19]. After solution annealing treatment, dynamic plastic deformation was conducted through the repetitive hammering method. Repetitive hammering with a strain rate of 6.2 s^{-1} on Cr-Mn austenitic stainless steels was carried out on five specimens with variations in the impact of 50, 100, 150, 250, and 350 times using 4.95 kg load mass as shown in the scheme in Fig. 1.

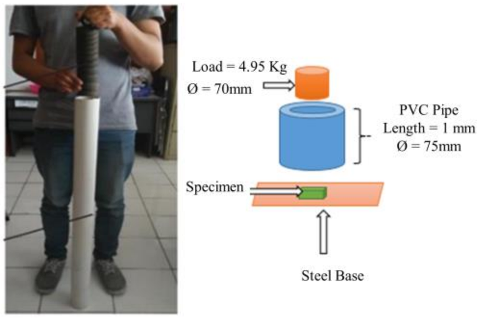

Figure 1. Repetitive hammering process

Hammering energy (E') and true strain (ε_t) on each specimen were calculated through equations (3) and (4). With, n = hammering cycle number, m = load (4.95 kg), g = gravity constant, h = Hammering drop height (1 m), dan s = specimen contact area, t_0= specimen's initial thickness, t_f= specimen's final thickness

$$E' = \frac{n.m.g.h}{s} \tag{3}$$

$$\varepsilon_t = ln\frac{t_0}{t_f} \tag{4}$$

Microstructure observation was conducted through the metallography examination. The specimens were polished and etched with aqua regia etchant to reveal their microstructure. Then, a hardness test was done with Rockwell A hardness test. Lastly, the XRD (x-ray diffraction) examination analyzed the specimen's existing phase.

3. RESULT AND DISCUSSION

The OES (optical emission spectroscopy) characterization results in Table 1, the material used belongs to the low alloy austenitic stainless-steel Cr-Mn. The composition of Ni as a stabilizer of austenite is relatively low, but the function of Ni is replaced by Mn so that the composition is relatively high. Reducing the composition of Ni by 1% must be replaced by adding 2% Mn to achieve austenite stability [20]–[24].

The Md_{30} and SFE (stacking fault energy) values are 99.2 °C and 0.0109 J/cm^2, respectively, indicating the very low possibility of martensite formation at room temperature during deformation [16].

Microplastic deformation marks and twinning were already observed on the as-received microstructure, indicating that the materials were already plastically deformed. Microplastic deformation twinning was successfully reduced with solution annealing treatment due to recrystallization, as shown in Fig. 2.

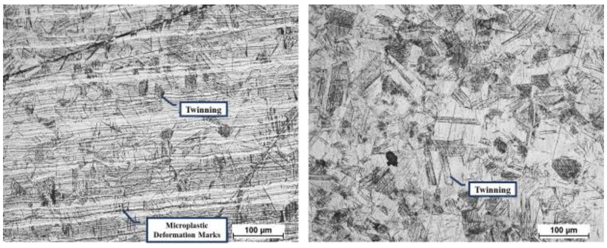

(a) (b)

Figure 2. Microstructure of (a) as received and (b) after solution annealing with aqua regia etchant low alloy austenitic stainless-steel Cr-Mn

Based on energy calculation and dimensional measurement on the austenitic stainless-steel Cr-Mn before and after repetitive hammering, more hammering from 50 to 350 cycles increase the hammering energy, reduce specimen thickness, and increase the true strain, as shown in Table. 2. Hammering energy achieved is much higher than the required (SFE) of materials (0.0109 J/cm^2) calculated using Equation 1.

Table 2. Hammering energy and true strain of low alloy austenitic stainless-steel Cr-Mn after repetitive hammering

Cycle (n)	Hammering Energy (J/cm^2)	Initial thickness (mm)	Final thickness (mm)	True Strain
50	486	9.30	9.00	0.03
100	2207		8.67	0.07
150	2569		8.14	0.13
250	6070		7.74	0.18
350	11330		6.88	0.30

Increased the true strain of materials is the primary indicator of a higher degree of plastic deformation due to higher hammering energy. After repetitive hammering, slip band and cross-band were observed on the microstructure of the 486 J/cm^2 hammering energy or 50 hammering cycle. The density of the slip band was increased along with the greater hammering energy. Furthermore, the wavy band was observed on austenitic stainless steel Cr-Mn microstructure that received higher hammering energy as in 150 Hammering Cycle (2569 J/cm^2 Hammering Energy) and 350 Hammering Cycle (11330 J/cm^2 Hammering Energy), while twinning phenomena were observed on all of austenitic stainless steel Cr-Mn. Slip bands and cross-band were easily formed on the austenitic stainless steel that received repetitive hammering due to its low SFE value; thus, both slip bands and cross-band will be formed on the material that experienced lower hammering energy [25]–[28].

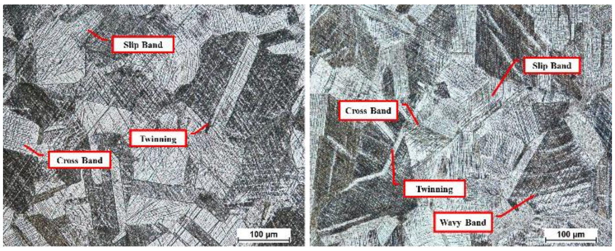

(a) (b)

Figure 3. Microstructure of 50 hammering cycle (486 J/cm^2 hammering energy) and (b) 150 hammering cycle (2569 J/cm^2 hammering energy) with aqua regia etchant

After repetitive hammering, plastic deformation on the specimen was confirmed by a metallography examination that showed a higher degree of slip-band and twinning inside the structure grain on the specimen that received higher hammering energy, as shown in Fig. 3 and Fig. 4.

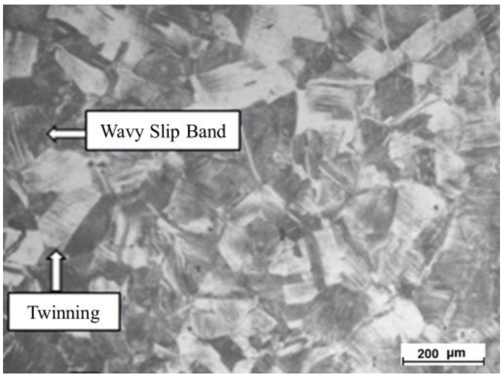

Figure 4. Microstructure of low alloy austenitic stainless-steel Cr-Mn 350 hammering cycle (11330 J/cm^2 hammering energy) with aqua regia etchant

In contrast, a higher SFE is needed to create a wavy band could explain why it is only observed on the higher hammering energy, such as on the 2569 J/cm^2 hammering energy.

The formation of the slip, cross, and wavy bands could obstruct the dislocation movement and cause strain hardening [29]–[31]. This phenomenon was observed in the hardness test result shown in Table 3. The hardness of the stainless steel that was already reduced due to solution annealing treatment from 58 to 53.5 HRA will be increased up to 71.6 HRA after the repetitive hammering process and following the increment of true strain, as shown in Fig. 5.

The XRD analysis in Fig. 6 shows a decreasing austenitic peak (γ-111) intensity from 907 at the as-received to 542 at the material with 350 hammering cycles (11030 J/cm2 hammering energy).

Table 3. Hardness test result of as received, after solution annealing and after repetitive hammering low alloy austenitic stainless-steel Cr-Mn

Specimen / Cycle (n)	Hammering Energy (J/cm^2)	True Strain	Hardness (HRA)
As Received	-	-	58±1.57
After Solution Annealing	-	-	53.5±0.85
50	486	0.03	54.3 ± 0.81
100	2207	0.07	58 ± 1.60
150	2569	0.13	62.2 ± 0.55
250	6070	0.18	67.6 ± 0.38
350	11330	0.30	71.6 ± 0.36

The decreased intensity indicated the formation of the lattice distortion that formed the slip band [11], [29], [32]-[33]. Also, with hammering energy of 2.207 J/cm2, the ε and α' martensite phases appear due to relatively low SFE value in the austenitic stainless steel Cr-Mn specimen (10.9 mJ/m2) with the strain rate of 6.2 s-1 [16].

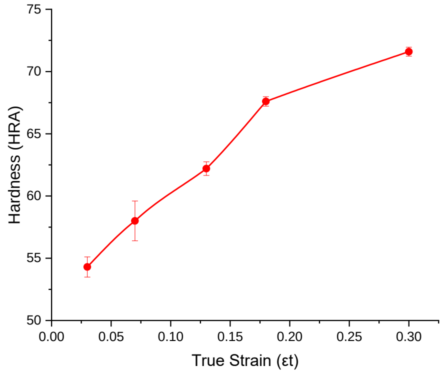

Figure 5. Hardness vs. true strain curve of low alloy austenitic stainless steel Cr-Mn after repetitive hammering

Also, with hammering energy of 2.207 J/cm^2, the ε and α' martensite phases appear due to relatively low SFE value in the austenitic stainless steel Cr-Mn specimen (10.9 mJ/m^2) with the strain rate of 6.2 s^{-1} [16].

Table 4 shows the impact energy of 11,330 J/cm^2, an increased FWHM (full width at half maximum) value from 0.452 to 0.483 compared to the initial material at hkl (111), indicates a widening and shift of the diffraction peaks caused by the formation of nano-twins measuring about 5 nm and the increasing density of stacking faults [33]-[34].

Nano-twin and stacking faults are planar defects that cause lattice parameters to change. Therefore, it causes a strain field to cause a shift and widening of the diffraction peak [9], [35]-[36].

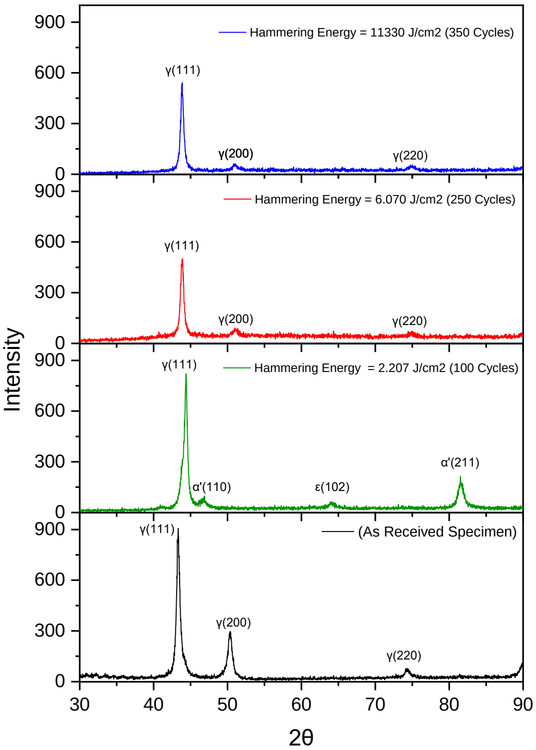

Figure 6. XRD result on as-received material, 100 hammering cycle (2207 J/cm^2 hammering energy), 250(6070 J/cm^2 hammering energy), and 350 hammering cycle (11330 J/cm^2 hammering energy) low alloy austenitic stainless-steel Cr-Mn

The formation of nano-twins can occur due to mechanical twinning in the repetitive hammering process.

Table 4. FWHM of as-received material, 100 hammering cycle (2207 J/cm^2 hammering energy), 250(6070 J/cm^2 hammering energy), and 350 hammering cycle (11330 J/cm^2 hammering energy) low alloy austenitic stainless steel Cr-Mn

Austenitic SS Cr-Mn Treatment	2θ	Hkl	FWHM
Solution annealing	43.4	(111)	0.452
	50.3	(200)	0.675
	74.4	(220)	1.024
Hammering energy 2207 J/cm^2	44.4	(111)	0.479
	46.9	(110)	-0.050
	64.0	(102)	1.066
	81.5	(211)	0.708
Hammering energy 6070 J/cm^2	43.9	(111)	0.411
	51.0	(200)	1.211
	74.9	(220)	0.921
Hammering energy 11330 J/cm^2	43.9	(111)	0.483
	51.0	(200)	1.538
	75.0	(220)	1.192

At the same time, the stacking faults can appear because the SFE value of the austenitic Cr-Mn stainless steel of 10.9 mJ/m^2 is relatively low. Thus, it is easier to form more stacking faults on the Cr-Mn austenitic stainless steel along with the given deformation widening of the diffraction peaks on the material from the repetitive hammering with the energy 11330 J/cm^2. The XRD analysis supports the microstructure analysis results. It shows that the increase in hardness in Cr-Mn austenitic stainless steels resulting from repetitive hammering is caused by strain hardening and an indication of mechanical twinning that forms nano-twin grains stacking faults. The sign of the presence of nano-twin shows the success of the dynamic plastic deformation process using repetitive hammering [33]-[34].

4. CONCLUSIONS

Repetitive hammering process up to 350 hammering cycles (11030 J/cm^2 hammering energy) can cause the formation of slip band, cross band, and wavy band with the indication of the nano-twin presence on the Cr-Mn austenitic stainless steel. The repetitive hammering process also increased the hardness from 53.5 HRA to 71.6 HRA, which shows the success of strengthening Cr-Mn austenitic stainless steel through the dynamic plastic deformation induced by repetitive hammering.

ACKNOWLEDGMENT

This research was financially supported by the Faculty of Mechanical and Aerospace Engineering, Institut Teknologi Bandung.

REFERENCES

[1] M. F. McGuire, *Stainless steels for design engineers*. Asm International, pp. 1 - 10; 69-90, 2008.

[2] A. Amininejad, R. Jamaati, and S. J. Hosseinipour, “Achieving superior strength and high ductility in AISI 304 austenitic stainless steel via asymmetric cold rolling,” *Mater. Sci. Eng. A*, vol. 767, pp. 138433, 2019.

[3] A. Di Schino, “Manufacturing and application of stainless steels,” *Manuf. Appl. Stainl. Steels*, pp. 7-9, 2020. Doi: 10.3390/books978-3-03928-651-5.

[4] D. Molnár, X. Sun, S. Lu, W. Li, G. Engberg, and L. Vitos, “Effect of temperature on the stacking fault energy and deformation behaviour in 316L austenitic stainless steel,” *Mater. Sci. Eng. A*, vol. 759, no. May, pp. 490-497, 2019. Doi: 10.1016/j.msea.2019.05.079.

[5] D. Xu, X. Wan, J. Yu, G. Xu, and G. Li, “Effect of cold deformation on microstructures and mechanical properties of austenitic stainless steel,” *Metals (Basel).*, vol. 8, no. 7, p. 522, 2018. Doi: 10.3390/met8070522.

[6] G. G. Maier and E. G. Astafurova, “A comparison of strengthening mechanisms of austenitic Fe-13Mn-1.3 C steel in warm and cold high-pressure torsion,” *Metals (Basel).*, vol. 10, no. 4, p. 493, 2020.

[7] F. K. Yan, G. Z. Liu, N. R. Tao, and K. Lu, “Strength and ductility of 316L austenitic stainless steel strengthened by nano-scale twin bundles,” *Acta Mater.*, vol. 60, no. 3, pp. 1059-1071, 2012.

[8] G. M. de Bellefon, J. C. Van Duysen, and K. Sridharan, “Composition-dependence of stacking fault energy in austenitic stainless steels through linear regression with random intercepts,” *J. Nucl. Mater.*, vol. 492, pp. 227-230, 2017.

[9] P. Uttam, V. Kumar, K. H. Kim, and A. Deep, “Nanotwinning: Generation, properties, and application,” *Mater. Des.*, vol. 192, pp. 108752, 2020. Doi: 10.1016/j.matdes.2020.108752.

[10] K. Lu, F. K. Yan, H. T. Wang, and N. R. Tao, “Strengthening austenitic steels by using nanotwinned austenitic grains,” *Scr. Mater.*, vol. 66, no. 11, pp. 878-883, 2012.

[11] S. Wang, K. Wei, J. Li, Y. Liu, Z. Huang, Q. Mao, and Y. Li, “Enhanced tensile properties of 316L stainless steel processed by a novel ultrasonic resonance plastic deformation technique,” *Mater. Lett.*, vol. 236, pp. 342-345, 2019. Doi: 10.1016/j.matlet.2018.10.080.

[12] A. K. Agrawal and A. Singh, “Limitations on the hardness increase in 316L stainless steel under dynamic plastic deformation,” *Mater. Sci. Eng. A*, vol. 687, pp. 306-312, 2017.

[13] H. T. Wang and N. R. Tao, “Nano-twinned Fe-Mn alloy prepared by reverse martensitic phase transformation,” *Scr. Mater.*, vol. 145, pp. 109-112, 2018. Doi: 10.1016/j.scriptamat.2017.10.024.

[14] J. Li, Y. Cao, B. Gao, Y. Li, and Y. Zhu, “Superior strength and ductility of 316L stainless steel with heterogeneous lamella structure,” *J. Mater. Sci.*, vol. 53, no. 14, pp. 10442-10456, 2018. Doi: 10.1007/s10853-018-2322-4.

[15] C. Haase, D. A. Molodov, and W. Bleck,

"Texture and microstructure evolution during deformation and annealing of high-manganese TWIP steels," Lehrstuhl und Institut für Eisenhüttenkunde, 2016.

[16] S.-J. Lee, Y. Sun, and H. Fujii, "Stacking-fault energy, mechanical twinning and strain hardening of Fe-18Mn-0.6 C-(0, 1.5) Al twinning-induced plasticity steels during friction stir welding," *Acta Mater.*, vol. 148, pp. 235-248, 2018.

[17] W. Bleck, X. Guo, and Y. Ma, "The TRIP effect and its application in cold formable sheet steels," *Steel Res. Int.*, vol. 88, no. 10, pp. 1700218, 2017.

[18] R. Kartikasari, A. E. Wijaya, A. D. Iskandar, S. Subardi, and T. Triyono, "Mechanical properties and corrosion resistance of grinding ball Fe-xMn-10Al-1.25C alloys," *J. Phys. Conf. Ser.*, vol. 1375, no. 1, 2019. Doi: 10.1088/1742-6596/1375/1/012076.

[19] G. Meric de Bellefon, M. N. Gussev, A. D. Stoica, J. C. van Duysen, and K. Sridharan, "Examining the influence of stacking fault width on deformation twinning in an austenitic stainless steel," *Scr. Mater.*, vol. 157, pp. 162-166, 2018. Doi: 10.1016/j.scriptamat.2018.08.012.

[20] J. Zhang, Y. He, Y. Wang, Y. Wang, and T. Wang, "Influence of annealing temperature on microstructure, tensile properties and tensile deformation mechanism of metastable austenitic stainless steel repetitively cold-rolled and annealed," *Materialia*, vol. 8, 2019. Doi: 10.1016/j.mtla.2019.100455.

[21] R. E. Smallman and R. J. Bishop, *Modern physical metallurgy and materials engineering*. Butterworth-Heinemann, pp. 221-224; 297-299, 1999.

[22] H. S. Noh, J. H. Kang, K. M. Kim, and S. J. Kim, "Different effects of Ni and Mn on thermodynamic and mechanical stabilities in Cr-Ni-Mn austenitic steels," *Metall. Mater. Trans. A Phys. Metall. Mater. Sci.*, vol. 50, no. 2, pp. 616-624, 2019. Doi: 10.1007/s11661-018-5042-0.

[23] H. S. Noh, J. H. Kang, K. M. Kim, and S. J. Kim, "The effects of replacing Ni with Mn on hydrogen embrittlement in Cr-Ni-Mn-N austenitic steels," *Corros. Sci.*, vol. 152, pp. 93-100, 2019. Doi: 10.1016/j.corsci.2019.03.012.

[24] M. Khorrami, A. Z. Hanzaki, H. R. Abedi, M. Moallemi, J. Mola, and G. Chen, "On the effect of Mn-content on the strength-ductility balance in Ni-free high N transformation induced plasticity steels," *Mater. Sci. Eng. A*, vol. 814, pp 141260, 2021. Doi: 10.1016/j.msea.2021.141260.

[25] H. L. Yan, Y. Zhao, H. X. Liu, M. J. Zhang, H. F. Zhang, J. Bai, N. Jia, B. Yang, Z. B. Li, Y. D. Zhang, C. Esling, X. Zhao, and L. Zuo, "Ab-initio revelation on the origins of Ti substitution for Ga, Mn and Ni on ferromagnetism, phase stability and elastic properties in Ni2MnGa," *J. Alloys Compd.*, vol. 821, pp. 153481, 2020. Doi: 10.1016/j.jallcom.2019.153481.

[26] A. Weidner, J. Man, W. Skrotzki, and J. Polák, "Slip localization and dislocation structure at early stages of fatigue damage in austenitic stainless steel (316L)," *ICF12, Ottawa*, vol. 2013, 2009.

[27] B. Poole and F. P. E. Dunne, "Slip band interactions and GND latent hardening in a galling resistant stainless steel," *Mater. Sci. Eng. A*, vol. 813, pp. 141176, 2021. Doi: 10.1016/j.msea.2021.141176.

[28] R. Ke, X. Wan, Y. Zhang, C. Hu, and K. Wu, "Insight in the impact of pre-deformation on structure - deformation - property relationship in Cr-Mn-N stainless steel," *Mater. Charact.*, pp. 111689, 2021. Doi: 10.1016/j.matchar.2021.111689.

[29] H. Kamali, H. Xie, H. Bi, E. Chang, H. Xu, H. Yu, and Z. Jiang, "Deformation mechanism and texture evolution of a low-Ni Cr–Mn–N austenitic stainless steel under bending deformation," *Mater. Sci. Eng. A*, vol. 804, pp. 140724, 2021. Doi: 10.1016/j.msea.2020.140724.

[30] A. A. Tiamiyu, V. Tari, J. A. Szpunar, A. G. Odeshi, and A. K. Khan, "Effects of grain refinement on the quasi-static compressive behavior of AISI 321 austenitic stainless steel: EBSD, TEM, and XRD studies," *Int. J. Plast.*, vol. 107, pp. 79-99, 2018. Doi: 10.1016/j.ijplas.2018.03.014.

[31] A. Grajcar, A. Kozłowska, and B. Grzegorczyk, "Strain hardening behavior and microstructure evolution of high-manganese steel subjected to interrupted tensile tests," *Metals (Basel).*, vol. 8, no. 2, 2018. Doi: 10.3390/met8020122.

[32] Y. Hong, C. Zhou, Y. Zheng, L. Zhang, J. Zheng, X. Chen, and B. An, "Formation of strain-induced martensite in selective laser melting austenitic stainless steel," *Mater. Sci. Eng. A*, vol. 740-741, pp. 420-426, 2019. Doi: 10.1016/j.msea.2018.10.121.

[33] P. Muhammed Shafi and A. Chandra Bose, "Impact of crystalline defects and size on X-ray line broadening: A phenomenological approach for tetragonal SnO2 nanocrystals," *AIP Adv.*, vol. 5, no. 5, pp. 57137, 2015.

[34] B. Roy and J. Das, "Strengthening face centered cubic crystals by annealing induced nano-twins," *Sci. Rep.*, vol. 7, no. 1, pp. 1-8, 2017.

[35] L. Löffler and W. Mader, "Anisotropic X-ray diffraction peak broadening and twinning in diaspore-derived corundum," *J. Eur. Ceram. Soc.*, vol. 25, no. 5, pp. 639-648, 2005.

[36] Z. Pei, "An overview of modeling the stacking faults in lightweight and high-entropy alloys: Theory and application," *Mater. Sci. Eng. A*, vol. 737, no. September, pp. 132-150, 2018. Doi: 10.1016/j.msea.2018.09.028.

[37] W. Woo, J. S. Jeong, D. Kim, C. M. Lee, S. Choi, J. Suh, S. Y. Lee, S. Harjo, and T. Kawasaki, "Stacking fault energy analyses of additively manufactured stainless steel 316L and CrCoNi Medium entropy alloy using in situ neutron diffraction," *Sci. Rep.*, vol. 10, no. 1, pp. 2-4, 2020. Doi: 10.1038/s41598-020-58273-3.

Metalurgi (2022) 1: 15 - 20

METALURGI
Majalah Ilmu dan Teknologi
p-ISSN 0126-3188 | e-ISSN 2443-3926
ejurnalmaterialmetalurgi.lipi.go.id

GRAIN GROWTH KINETICS OF AUSTENITIC STAINLESS STEEL 316L AND THE RELATIONS BETWEEN GRAIN SIZES AND HARDNESS UNDER ISOTHERMAL CONDITIONS

Moch Syaiful Anwar[a, b]*, Mayang Gita Pradisti[a], Septian Adi Candra[b], Erie Martides[c], Efendi Mabruri[b], Eddy Sumarno Siradj[a]
[a]Department of Metallurgical and Materials Engineering, University of Indonesia
Kampus UI Depok, Jawa Barat, Indonesia, 16424
[b]Research Center for Metallurgy, National Research and Innovation Agency
Gedung 470, Kawasan Puspiptek Serpong, Banten, Indonesia, 15314
[c]Research Center for Electric Power and Mechatronics, National Research and Innovation Agency
Gedung 20, Jl. Sangkuriang, Bandung, Jawa Barat, 40135
*E-mail: msyifulan04@gmail.com

Received : 16-02-2022, Revised : 02-06-2022, Accepted : 23-06-2022

Abstract

The 316L austenitic stainless steel is usually used in nuclear power plant. This steel has an austenitic phase at room temperature, and it can change grain size after being exposed at high temperatures. This study aims to investigate grain growth behavior and hardness of 316L austenitic stainless steel after cold-rolled and annealing to 1100 °C with holding times of 0, 900, 1800, 2700, 3600 s. The result showed that the grain growth of 316L austenitic stainless steel usually occurs. Austenite grain size of 316L increased with increasing holding time, resulting in hardness decreases. Experimental grain growth of 316L austenitic stainless steel shows no significant difference from the prediction, with an error of about 0.7. The highest Micro Vickers hardness is found at a grain size of 14.93 µm.

Keywords: *Austenitic stainless steel 316L, grain growth kinetics, hardness, modeling*

1. INTRODUCTION

Due to its mechanical properties such as high tensile strength, good ductility, and high corrosion resistance, 316L austenitic stainless steel has many applications in industry and is commonly used as a structural material in nuclear power plants [1]. Austenite grain size and microstructure grain growth play an important role in determining mechanical properties [2]. For example, the hardness of steel decreases with increasing grain size. To increase the material's hardness, the grain boundaries must be increased to make the grains as small as possible. Grain boundaries prevents movement of dislocations due to lack of continuity of the slip plane from one grain to another, and dislocations propagating to other grains must change the direction of movement [3].

Previous studies have been conducted on grain growth in austenitic stainless steels. Järvenpaa et al., [4] found that the finer the grain size of austenitic stainless steels, the higher the yield strength. Li et al., [5] studied the effect of cold rolling on the mechanical properties of 304N stainless steel. They found that the higher the cold reduction, the more strained martensite was formed, which increased strength but decreased elongation. Bedjati et al., [6] studied the effect of annealing temperature on the grain size of austenitic stainless steel Ni-free. They used cold rolling with a high rolling reduction of about 80% and then reverse annealed at 900 °C for 100 seconds to obtain ultra-fine and nano-sized austenite grain. Nano/ultra-fine grain size provides ultra-high-strength and excellent elongation. Jiang et al., [7] investigated the

DOI : 10.14203/metalurgi.v37i1.629

Metalurgi is Sinta 2 Journal (https://sinta.ristekbrin.go.id/journals/detail?id=3708) accredited by Ministry of Research & Technology, Republic of Indonesia

microstructure and mechanical properties of high nitrogen austenitic stainless steel after aging at 900 °C for 0 to 50 hours. They stated that the presence of intergranular Cr_2N precipitation caused the Vickers hardness value to decrease and the Vickers hardness value to increase due to increased Cr_2N precipitation, the formation of cellular Cr_2N, and the intermetallic phase. Thikonova et al., [8] stated that the strength of metallic materials increases with ductility decreases. The controlled thermomechanical treatment includes post-deformation annealing resulting in a beneficial effect on the microstructure. Wang et al., [9] presented an air-coupled probe for grain size characterization of 316L stainless steel using Rayleigh wave attenuation. Matt et al., [10] stated that the Arrhenius equation could predict the grain size of austenitic stainless steels by examining the behavior of materials at high temperatures. It was argued that the appearance of abnormal grain in the high-temperature region would absorb the surrounding grain, and the sediments generated at the grain boundary could be realized through the modified Arrhenius equation.

However, to the best of the author's knowledge, studies on grain growth of 316L austenitic stainless steels due to cold rolling under low reduction have not yet been conducted. This study was designed to predict austenite grain size using the grain growth equation and the relationship between hardness and grain size.

2. MATERIALS AND METHODS

In this experiment, Steel SS316L was used. Table 1 shows the chemical composition of the steel. The steel was cold-rolled with a reduction of 22%. It is then heated in a tube furnace using gaseous hydrogen at a temperature of 1100 °C and at a heating rate of 5 °C/min with holding times of 900, 1800, 2700, and 3600 s before quenching in the cooling zone.

The microstructure was observed in the steel sample using an optical microscope. The steel is polished by conventional metallographic methods and etched in aqua regia (80% HCl and 20% HNO_3) for 1 min to reveal the boundaries of the austenite grains. Austenite grain size was determined by the mean linear intercept method. A hardness test was then performed on a Vickers micromachine with a load of 0.3 N.

Tabel 1. Chemical composition of 316L ASS (wt.%)

C	Si	Mn	P	S	Ni	Cr	Mo	Fe
0.012	0.3	1.67	0.035	<0.005	9.45	17.33	2.1	Bal.

3. RESULTS AND DISCUSSION

Figure 1 shows the microstructure of austenite grain of 316L after 22% reduction of cold rolling. This figure shows that the grain is not elongated after cold rolling, and many precipitates showed a dot in black spread out in the austenite matrix and grain boundary.

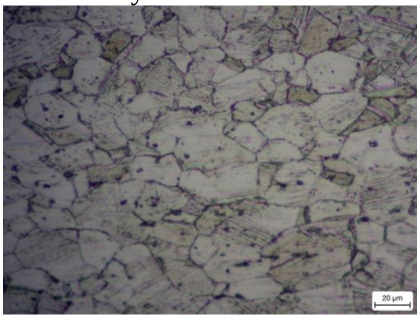

Figure 1. Microstructure of austenite grain boundaries of SS 316L after cold rolling. Aqua regia etchant

Figures 2(a)-2(e) reveal that the annealing twin formed in each condition.

Table 2. Grain size of SS 316L under different holding time at 1100 °C

Holding time (s)	0	900	1800	2700	3600
Grain size (µm)	14.93	23.56	26.18	28.97	29.28

Annealing twin occurs due to the cold-rolling process followed by heat treatment as a result of rearranging the atoms during the grain growth process [11].

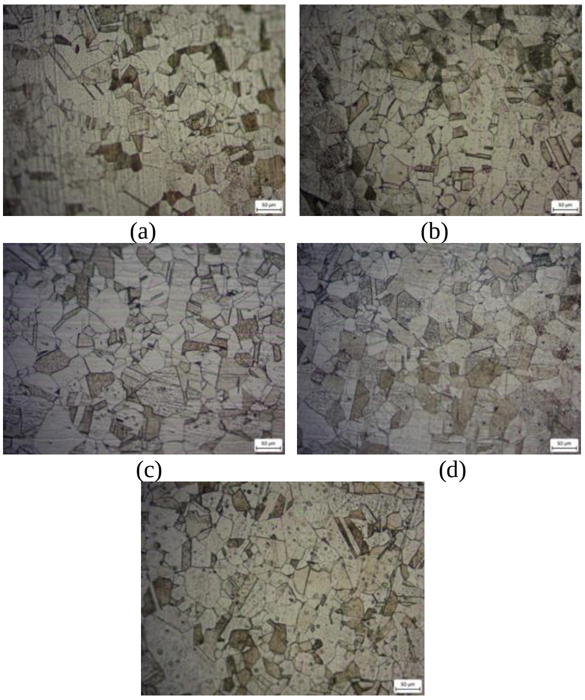
(a) (b) (c) (d) (e)

Figure 2. Microstructure of austenite grain boundaries under different heat treatment conditions of SS 316L at 1100 °C with the time (s); (a) 0, (b) 900, (c) 1800, (d) 2700, (e) 3600. Aqua regia etchant

Grain sizes for all annealing conditions are given in Table 2.

The results show that SS 316L grains grow as the holding time increases. Figure 3 depicts the experimental results for changes in grain size under all annealing conditions.

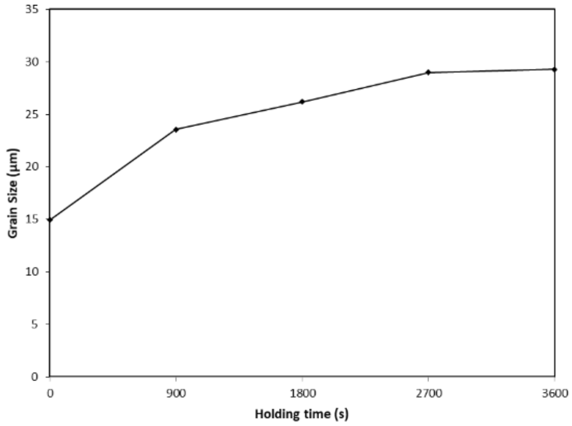

Figure 3. Austenite grain size of SS 316L under different holding times at 1100 °C

Table 3 shows experimental results on grain sizes and hardness of SS 316L annealed under different holding times at 1100 °C.

Table 3. Experimental result on grain size and hardness of SS 316L annealed under different holding time at 1100 °C

Holding time (s)	**0**	**900**	**1800**	**2700**	**3600**
Hardness micro-Vickers (HV)	149,4	148,6	148,1	147,3	146,8

Figure 4 shows that the hardness of the steel increases as the grain refinement degree increases. ($d^{-0.5}$). It is because steels with small grain sizes have more grain boundaries, inhibiting the dislocation movement. Hence, it is difficult for the dislocation to move because it needs more energy to move across the grain boundary due to differences in atomic orientation. The data were obtained by the Hall-Petch relationship, that the hardness of the annealed steel decreases with grain size increases [12].

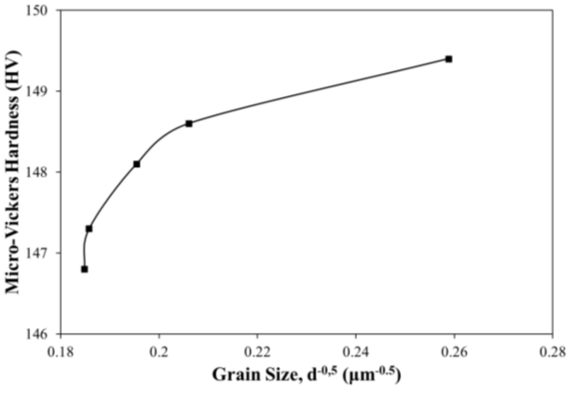

Figure 4. Relationship between grain size, $d^{-0,5}$ and hardness value in SS 316L

Figure 5 compares the hardness value of SS 316L in this study to other steels based on previous research. The hardness of most steels increases as the value of d-0.5 grain size increases. The steel type also influences the hardness value. Stainless steel 316L, for example, has a higher hardness value than FeCoNiMn but a lower hardness value than FeCoNiCrPd steel, 253 MA, FeCo-NiCrMn, and CoNiMn. It means that a high concentration of Cr, W, V, Mo, Ti, Nb, and Mn can increase steel hardness on the exact value of $d^{-0.5}$ grain size [13].

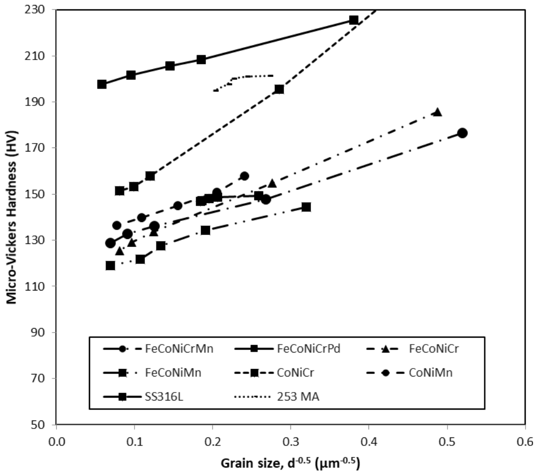

Figure 5. Hardness value of different type of steel under different annealing condition

Different pre-treatment and annealing treatments can result in an other kind of precipitate and affect the hardness of steel [12].

The average grain growth of steel is often expressed by the following empirical Equation 1 [14].

$$D^n = Kt \tag{1}$$

Where D is the average grain size at time t, t is holding time, n is the grain growth exponent, and K is the temperature dependence. The value of n depends on the grain growth mechanism [15]. Based on the basic theory of grain growth, the predicted values of n are usually greater than or equal to 2 [16]. However, previous studies indicated that the value of n for austenitic stainless steel is around 0.128 to 0.443 [17].

Equation 1 describes the nature of grain growth when D is greater than the initial grain size (D_0). However, the neglect of D_0 can affect the value of the grain growth exponent. So, the influence of D_0 on the grain growth behavior should be considered, and the equation was developed in Equation 2.

$$D^n - {D_0}^n = Kt \tag{2}$$

The relationship between the constant K and temperature follows the Arrhenius equation in Equation 3.

$$K = K_0 exp(-\frac{Q_{gg}}{RT}) \qquad (3)$$

Where K_0 is the experimental parameter, Q_{gg} is the activation energy of grain growth, R is the molar gas constant of 8.314 J/molK, and T is the heating temperature.

Equations 2 and 3 can be combined to form a new equation as expressed in Equation 4.

$$D^n - {D_0}^n = K_0 exp(-\frac{Q_{gg}}{RT})t \qquad (4)$$

The grain growth activation energy (Q_{gg}) of SS316L steel used in this study was data from the Barbosa study with a Qgg value of 320,000 [18].

Equation 5 was obtained by the logarithmic transformation of Equation 4.

$$\ln(D^n - {D_0}^n) = lnK_0 - \frac{Q_{gg}}{RT} + lnt \qquad (5)$$

The constant values of n and K_0 are calculated with Microsoft Excel's Solver. As a result, the optimal values for n and K0 are 5.78 and $1.35\text{x}10^{17}$. The value of n in this study is similar to the basic grain growth theory. The difference between the simulated value and the study result is determined by calculating the SSE (sum of squares error). The resulting SSE value is 0.7. This indicates that the simulation error value is 0.7, and the simulation is close to the study results. Then, the empirical model of steel grain growth can be expressed as Equation 6.

$$D^{5,78} - {D_0}^{5,78} = 1,35 \times 10^{17} exp(-\frac{320.000}{RT})t \qquad (6)$$

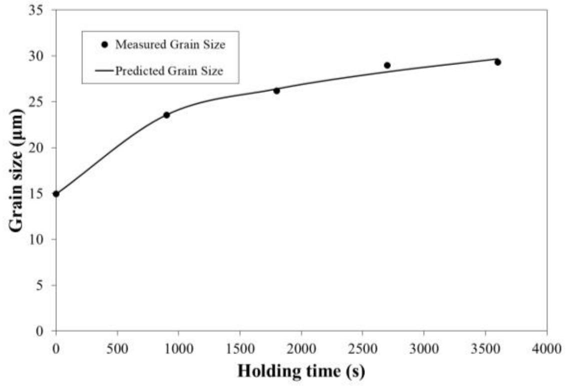

Figure 6. Comparison grain size resulting from experiment and prediction in SS 316L

Figure 6 is a comparison of the measured grain size and the predicted grain size. This figure shows that the measured grain size strongly conforms with the modeling results. The research model produces a sloping graph, and it is because the research model has a significant value of n. An important value of n indicates the resistance due to sediments that impede grain growth. As the value of n increases, the simulation graph is skewed, indicating that the grain growth rate is not constant and the grain growth rate is decreasing. The constant value of K0 depends on the composition and process of the steel [19]. Therefore, the obtained n and K0 constant values can predict grain growth of 316L austenitic stainless steel after cold rolling with a 22% reduction.

4. CONCLUSION

From the test results, it can be concluded that the effect of annealing holding time on the grain growth behavior and hardness of SS316L after low reduction cold rolling can be concluded: Growth of austenite grains usually occurs with longer holding times. When the annealing holding time was lengthened, the crystal grain size became slightly coarser, and the hardness decreased somewhat. The slight difference in crystal grain size and hardness at each annealing holding time is due to the slight reduction in cold rolling of 316L austenitic stainless steel. An empirical formula for predicting austenite grain growth at different retention times is obtained, and the prediction results end the experiment with an error of 0.7.

ACKNOWLEDGMENT

The author would like to thank the Universitas Indonesia and the National Research and Innovation Agency for their financial support. The experiment was carried out at Research Center for Metallurgy National Research and Innovation Agency.

REFERENCES

[1] M. El-Tahawy, Y. Huang, T. Um, H. Choe, J. L. Labar, T. L. Langdon, J. Gubizca, "Stored energy in ultrafine-grained 316L stainless steel processed by high-pressure torsion," *Journal of Materials Research and Technology*, vol. 6, no. 4, pp. 339-47, 2017. Doi: 10.1016/j.jmrt.2017.05.001.

[2] S. Illescas, J. Fernández, and J. M. Guilemany, "Kinetic analysis of the austenitic grain growth in HSLA steel with a low carbon content," *Materials*

Letters, vol. 62, no. 20, pp. 3478-3480, 2008. Doi: 10.1016/j.matlet.2008.03.001.

[3] W. D. Callister and D. G. Rethwisch, *Materials Science and Engineering, An Introduction*, 7th ed. John Wiley & Sons, Inc, pp. 229-243, 2007.

[4] A. Järvenpää, M. Jaskari, A. Kisko, and P. Karjalainen, “Processing and properties of reversion-treated austenitic stainless steels,” *Metals (Basel)*, vol. 10, no. 2, 2020. Doi: 10.3390/met10020281.

[5] X. Li, Y. Wei, Z. Wei, and J. Zhou, “Effect of cold rolling on microstructure and mechanical properties of AISI 304N stainless steel,” *IOP Conference Series: Earth and Environmental Science*, vol. 252, pp. 022027, 2019. Doi: 10.1088/1755-1315/252/2/022027.

[6] P. Behjati, A. Kermanpur, A. Najafizadeh, and H. S. Baghbadorani, “Effect of annealing temperature on nano/ultrafine grain of Ni-free austenitic stainless steel,” *Materials Science and Engineering: A*, vol. 592, pp. 77-82, 2014. Doi: 10.1016/j.msea.2013.10.087.

[7] Z. Jiang, Z. Zhang, H. Li, Z. Li, and M. Qi-feng, “Microstructural evolution and mechanical properties of aging high nitrogen austenitic stainless steels,” *International Journal of Minerals, Metallurgy, and Materials*, vol. 17, no. 6, pp. 729-736, 2010. Doi: 10.1007/s12613-010-0381-x.

[8] M. Tikhonova, R. Kaibyshev, and A. Belyakov, “Microstructure and mechanical properties of austenitic stainless steels after dynamic and post-dynamic recrystallization treatment,” *Advanced Engineering Materials*, vol. 20, no. 7, pp. 1700960, 2018. Doi: 10.1002/adem.201700960.

[9] M. Wang, Y. Bu, Z. Dai, and S. Zeng, “Characterization of grain size in 316L stainless steel using the attenuation of rayleigh wave measured by air-coupled transducer,” *Materials*, vol. 14, no. 8, 2021. Doi: 10.3390/ma14081901.

[10] M. F. Mat, Y. H. P. Manurung, N. Muhammad, S. N. S. Ahmad, M. Graf, and M. Shahar, “Variable analysis for grain size prediction of austenitic stainless steel SS316L using heat treatment,” *Journal of Applied Sciences*, vol. 20, pp. 91-96, 2020. Doi: 10.3923/jas.2020.91.96.

[11] Q. Xue, E. K. Cerreta, and G. T. Gray, “Microstructural characteristics of post-shear localization in cold-rolled 316L stainless steel,” *Acta Materialia*, vol. 55, no. 2, pp. 691-704, 2007. Doi: 10.1016/j.actamat.2006.09.001.

[12] Y. C. Huang, C. H. Su, S. K. Wu, and C. Lin, “A study on the Hall–Petch relationship and grain growth kinetics in FCC-structured high/medium entropy alloys,” *Entropy*, vol. 21, no. 3, 2019. Doi: 10.3390/e21030297.

[13] M. K. Banerjee, “2.1 Fundamentals of heat treating metals and alloys,” in *Comprehensive Materials Finishing*, M. S. J. Hashmi, Ed. Oxford: Elsevier, pp. 1-49, 2017. Doi: 10.1016/B978-0-12-803581-8.09185-2.

[14] R. Ren, Y. Wu, W. Tang, F. Wang, T. Wang, and Z. Zheng, “Synthesis and grain growth kinetics of in-situ FeAl matrix nanocomposites (II): Structural evolution and grain growth kinetics of mechanically alloyed Fe-Al-Ti-B composite powder during heat treatment,” *Transactions of Nonferrous Metals Society of China*, vol. 18, no. 1, pp. 66-71, 2008. Doi: 10.1016/S1003-6326(08)60012-6.

[15] C. Yue, L. Zhang, S. Liao, and H. Gao, “Kinetic analysis of the austenite grain growth in GCr15 steel,” *Journal of Materials Engineering and Performance*, vol. 19, no. 1, pp. 112-115, 2010. Doi: 10.1007/s11665-009-9413-y.

[16] W. D. Callister and D. G. Rethwisch, *Materials Science and Engineering, An Introduction.*, 7th ed. John Wiley & Sons, Inc., pp. 200, 2007.

[17] L. Gavard, F. Montheillet, and J. le Coze, “Recrystallization and grain growth in high purity austenitic stainless steels,” *Scripta Materialia*, vol. 39, no. 8, pp. 1095-1099, 1998. Doi: 10.1016/S13596462(98)00276-0.

[18] R. A. N. M. Barbosa, “Simulation of hot working of austenitic stainless steels,” University of Sheffield, pp. 35, 1983.

[19] D. Priadi, R. A. M. Napitupulu, and E. Siradj, “Austenite grain growth calculation of 0.028% nb steel,” *Journal of Mining and Metallurgy, Section B: Metallurgy*, vol. 47, 2011. Doi: 10.2298/JMMB100901001P.

Metalurgi (2022) 1: 21 - 30

METALURGI
Majalah Ilmu dan Teknologi
p-ISSN 0126-3188 | e-ISSN 2443-3926
ejurnalmaterialmetalurgi.lipi.go.id

EFFECTIVENESS OF THE SEPARATION OF MAGNESIUM AND LITHIUM FROM SEAWATER WITH SODIUM SILICATE PRECIPITATION PROCESS

Eko Sulistiyono[a,*], Sri Harjanto[a], Latifa Hanum Lalasari[b], Florentinus Firdiyono[b], Nadia Chrisayu Natasha[b], Yosephin Dewayani[b]
[a]Departments of Metallurgical and Materials Engineering, Universitas Indonesia,
Kampus UI Depok, Jawa Barat, Indonesia, 16425
[b] Research Center for Metallurgy, National Research and Inovation Agency (BRIN)
Gedung 470, Kawasan Puspiptek Serpong, Banten, Indonesia, 15314
*E-mail: eko221068@gmail.com

Received : 18-04-2022, Revised : 13-05-2022, Accepted : 23-06-2022

Abstract

The purpose of this experiment was to separate magnesium ions and lithium ions from seawater in order to obtain a lithium concentrate solution product free of magnesium using a sodium silicate precipitation process. The sample used in this experiment was seawater from the Ancol Lagoon Area in North Jakarta. The seawater used has a high Mg/Li ratio of 10521 and contains 0.1674 ppm lithium ions and 1761 ppm magnesium ions. Before initial processing, seawater with high magnesium levels is not suitable as a raw material for the manufacture of lithium carbonate (active battery ingredient). The variables in the study were the addition of sodium silicate solution in amounts corresponding to 13, 27, 40, 53, 67, 80, 93, and 107% stoichiometry of magnesium ion. One step and multiple stages were used to add sodium silicate solution. The experimental results show that the addition of sodium silicate with 80% stoichiometry is the most effective, as indicated by a decrease in the Mg/Li ratio from 10521 to 64. The limitation of this study is that many lithium ions are still precipitated with magnesium silicate during the precipitation process, so the lithium ions lost in the filtrate reached 82.26% in the single-stage process. As a result, a multi-stage process with six processing steps was used. At single-stage optimum conditions, the sodium silicate addition was 1/6 of the volume of sodium silicate solution. The multi-stage process results could reduce lithium-ion loss in the filtrate from 82.26% to 76.54%. According to the findings of this study, the sodium silicate precipitation process was ineffective in separating lithium and magnesium ions from seawater in both single and multi-stage processes.

Keywords: *Magnesium ion separation, lithium ion separation, sodium silicate residue, seawater*

1. INTRODUCTION

Seawater in unlimited quantities is one of the future natural resource potentials. The volume of seawater in the hemisphere is estimated to be 1.3 x 10^{18} tons, with a mineral content of 3.3%. Thus, the amount of minerals found in seawater around the world is estimated to be 3 x 10^{16} tons [1]. According to data from the 2015 USGS Mineral Commodity Summaries, the following cations are eligible for development from seawater mineral resources: Na, Ca, Mg, K, Li, Sr, Br, B, and U [1]. Based on the analysis of samples from various seawater regions around the world, the lithium potential is estimated to be 230 billion tons. While the world's known lithium reserves on land total only 14 million tons [2], When lithium reserves are compared, the ocean has 16,429 more lithium reserves than the land.

To ensure the availability of lithium raw materials, lithium extraction process technology must be developed while considering the potential of lithium from seawater resources. The adsorption method is commonly used in the research and development of lithium raw materials from marine natural resources. In contrast, lithium research and development on land typically employs the precipitation method for brine water and an alkaline digester for rocks [3]. One of the seawater lithium extraction studies using the adsorption method is manganese dioxide-based adsorbs. Research with

DOI : 10.14203/metalurgi.v37i1.640

Metalurgi is Sinta 2 Journal (https://sinta.ristekbrin.go.id/journals/detail?id=3708) accredited by Ministry of Research & Technology, Republic of Indonesia

manganese adsorption materials includes: adsorbing with sieve $MnO_2.0,5\ H_2O$ [4], with a mixture of lithium manganese dioxide and chitosan granules [5] and using λ -MnO_2 material in the form of hexagonal crystals [6]. The results of the three experiments showed that the adsorption capacity for the combination of MnO_2 with chitosan was 54.65 mg/g Li+ ions [5], the λ -MnO_2 hexagonal crystalline material was 24.7 mg/g Li+ ions [6]. The sieve MnO_2 ion material, 5 H_2O is 10.05 mg/g Li+ ion [4]. In addition to the adsorption process, a continuous electrical pumping membrane process was developed with the results of increasing the lithium concentration from 0.1-0.2 ppm to 9013.43 ppm [7]. The electrolysis process using the Pulsed Electrochemical Intercalation method obtained lithium ion selectivity results of 1.8 x 104 [8], the process two-stage precipitation using NaOH, Na_2CO_3, and HCl with the product yield of Li_2CO_3 content above 99% [9] and the separation process using metal aluminum foil [10].

Indonesia, a maritime country in the form of an archipelago, has the second longest beach in the world [11]. Therefore, mastery of seawater treatment technology into useful products must be done. Currently, the use of mineral resources from seawater in Indonesia is only in salt production. The total salt production in Indonesia from 44 regions in Indonesia was 2,915,461.17 tons in 2016 [11]. Until now, there has been no use of seawater in Indonesia to produce lithium carbonate products. Constraints faced in the process of extracting lithium from seawater resources are the very high ratio of lithium to magnesium (ratio Mg/li) and low levels of lithium from seawater. For example, the lithium content of seawater on the Lamongan beach is 0.17 ppm [12]. Based on the theory, with a low lithium content of about 0.18 ppm and an Mg/li ratio above 7000, it is challenging to be economically processed into lithium carbonate products [13].

In this research, the process of separating lithium ions and magnesium ions from seawater will be carried out using the sodium silicate precipitation process. In previous experiments with bittern as raw material from salt pond waste, the results obtained were only able to take up about 20% lithium ions, and the Mg/Li ratio was 1033 [12]. The precipitation process is one of the most straightforward and most practical lithium and magnesium ion separation processes [14]. In several methods, separating lithium ions and magnesium ions in brine water with the precipitation process showed promising results. The separation process for lithium and magnesium ions includes the precipitation process with the following materials: aluminum metal powder and sodium sulfate [15], oxalic acid and sodium carbonate with brine water Bledug Kuwu as raw material [16], ammonium phosphate for lithium anolyte concentrate as raw material [17], and the precipitation process with sodium metasilicate as precipitating agent [18].

The separation of magnesium ions and lithium ions will do to obtain a filtrate containing only lithium ions and no magnesium ions. This filtrate will be use as a raw material in the production of lithium carbonate. Lithium carbonate is a key ingredient in the production of lithium batteries.

2. MATERIALS AND METHODS

In this experiment, the precipitation process carried out the separation of lithium ions and magnesium ions in seawater. In this study, the principle of separating lithium ions and magnesium ions in seawater is the process of precipitation of magnesium ions with sodium silicate to produce magnesium silicate deposits. The reaction of sodium silicate with magnesium ion occurs in various possibilities, based on a literature study on the reaction of sodium silicate with magnesium ion as in the manufacture of synthetic talc, by reaction [19].

$$4\ (Na_2SiO_3) + 3\ (MgCl_2) + 2\ HCl + m\ H_2O == Si_4Mg_3O_{11}.n\ H_2O + 8\ NaCl + (m\text{-}n\text{+}1)H_2O \quad (1)$$

From reaction (1), a solid magnesium silicate and a filtrate free of magnesium ions were obtained. The effectiveness of the precipitation process can be seen from the decrease in the ratio of Mg/li ions in the filtrate due to a decrease in magnesium ions in the filtrate. In addition to reducing the ratio of magnesium to lithium ions, the percentage of lithium ions removed in the filtrate was also considered. The rate of lithium ions lost is formulated as follows:

$$X\ (\%) = \{(A – B)/A \} * 100\ \%\ \ ……… (1)$$

Descriptions:

X = Percentage ion remove
A = Mass ion in Raw Material
B =Mass ion in Filtrate after precipitation of sodium silicate

2.1 Materials

In this experiment, the seawater was taken from the Ancol Beach Lagoon, Jakarta, Indonesia. The ICP-OES (inductively coupled plasma-optical emission spectroscopy) analysis was carried out to identify seawater's chemical composition of seawater as shown in Table 1.

The precipitant was a sodium silicate solution derived from this study's water glass dilution process. The water glass used was sold in the market as a very thick solution containing a high concentration of sodium silicate.

Tabel 1. Chemical composition of seawater and sodium silicate (ppm)

Element	Seawater	Sodium Silicate
Magnesium (Mg)	1761	37.73
Sodium (Na)	4932	27126
Lithium (Li)	0.1674	-
Potassium (K)	243	201
Calcium (Ca)	421	54
Boron (B)	5,16	131
Ratio Mg/li	10521	-

2.2 Methods

In this experiment, the seawater performed a filtration process to remove solid impurities. The seawater of Jakarta Bay has high levels of nitrate, phosphate, and excessive algae growth [20]. In the filtration process, sufficient activated carbon was added to seawater to obtain clear seawater. After getting a clear solution, the precipitation process was prepared.

The precipitation process was carried out by adding sodium silicate solution calculated based on the stoichiometry of the magnesium ion. The stoichiometric variables are 13, 27, 40, 53, 67, 80, 93, and 107%. Precipitation experiments with sodium silicate solution were carried out at room temperature (without heating), a processing time of 5 minutes, and a stirring speed of 300 rpm. After the precipitation process was carried out, the residual solid and filtrate were obtained, and then the separation process was carried out. The filtrate obtained was then measured in volume and analyzed for ion concentration using ICP-OES. The solids obtained are then measured by weight, and the drying process is carried out. The obtained solids were then analyzed by XRD (x-ray diffraction). After analyzing the filtrate and solids, the data was investigated to get the best condition of the experiment.

In the sodium silicate precipitation experiment, two processes were carried out, namely single-stage and multi-stage processes (Figure 1). In the first stage, a single-stage process is carried out, namely the sodium silicate precipitation process which is given in one stage of the process. After knowing the optimum conditions for the single-stage process with the addition of 80% stoichiometric sodium silicate, a multistage process was carried out under these conditions. In this experiment, the multistage process was carried out six times. The addition of sodium silicate at each stage of the multistage process is 1/6 of 80% stoichiometric sodium silicate. So that each stage was added 13.33 % stoichiometric sodium silicate.

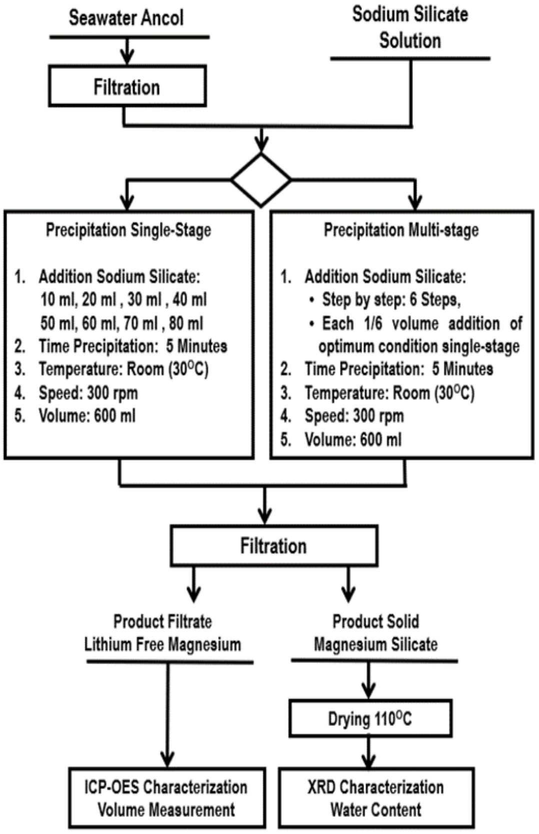

Figure 1. The progression of stage in this study

Based on the data from the ICP-OES analysis before the precipitation process (Table 1) and the ICP-OES analysis after the precipitation process (Table 3), a comparison ratio of elemental concentrations can be made. The formula for the ratio of the concentration of elements is as follows:

$R = (CA / CB)$ …………………. (2)

Descriptions:
R = Ratio Concentration
CA = Concentration Filtrate Product
CB = Concentration seawater

3. RESULT AND DISCUSSION

3.1 Single-Stage Process

Magnesium ions in seawater react with sodium silicate to form a white precipitate during the separation of magnesium ions and lithium ions from seawater. The white precipitate is formed by the reaction of magnesium ions and silicate ions, which results in the formation of a new compound of magnesium silicate that is insoluble in water.

3.1.1 Ratio Mg/Li in Filtrate after Precipitation

The sodium silicate precipitation process was carried out in this study with variable sodium silicate addition. Figure 2 depicts the effect of sodium silicate on the Mg/Li ratio. In addition to up to 40% sodium silicate, the stoichiometric separation of lithium-ion and magnesium ions did not produce an effective separation. This is due to the lack of a significant decrease in the Mg/Li ratio. With the addition of 40% stoichiometric sodium silicate, the Mg/Li ratio increased to 11417.

With more than 40% stoichiometric sodium silicate, the Mg/Li ratio decreased to 3426; with 53% stoichiometric sodium silicate, the Mg/Li ratio decreased to 306; and with 67% stoichiometric sodium silicate, the Mg/Li ratio decreased to 306 (Fig 2).

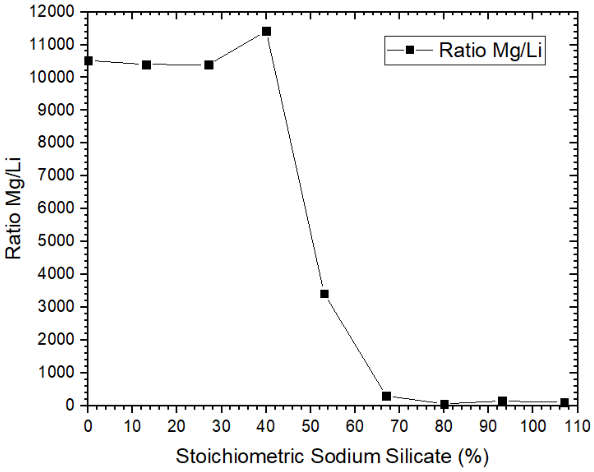

Figure 2. Effect of the addition of sodium silicate on the Mg/Li ratio in the single-stage precipitation process

The Mg/Li ratio dropped to 3426 with more than 40% stoichiometric sodium silicate. The Mg/Li ratio was reduced to 306 after the addition of 53% stoichiometric sodium silicate and then 67% stoichiometric sodium silicate (Fig 2). The addition of 60 mL sodium silicate, or 80% stoichiometry, produced the best results; the Mg/Li ratio was 64. The Mg/Li ratio did not fall below 64 in the sodium silicate range of 80% stoichiometric to 107% stoichiometric. Instead, it was increased to 152 by adding 93% stoichiometric sodium silicate (Fig 2). According to the experimental results, the Mg/Li ratio decreases not only as a result of reduced magnesium ions in the filtrate, but also as a result of reduced lithium ions in the filtrate.

3.1.2 The Percentage of Ion Removal in Filtrate after Precipitation (Single-Stage)

The sodium silicate precipitation process, which can reduce the Mg/Li ratio from 10521 to 64, opens the door to the possibility of extracting lithium from seawater. Previous research concluded that lithium resources with Mg/Li ratios greater than 7000 are impossible to extract [13].

In addition to the Mg/Li ratio factor, the mass percentage of lithium ions removed from the filtrate after the precipitation process is shown. The sodium silicate precipitation experiment results show that the concentration of lithium ions and magnesium ions decreases as magnesium ions precipitate to form magnesium silicate solids. The experimental results with the variable addition of sodium silicate show that the addition of sodium silicate up to 40% increases the mass removal of lithium and magnesium ions. With the addition of 40% stoichiometric sodium silicate, the number of lithium ions removed increased to 74.93% and magnesium ions decreased to 72.79%. (Fig 3).

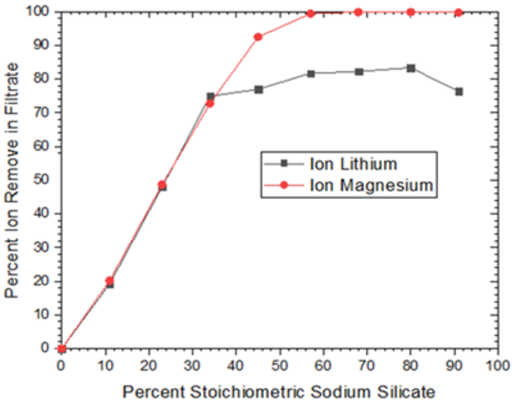

Figure 3. Effect of the addition of sodium silicate on the percent ion remove infiltrate in the single-stage precipitation process

The precipitated magnesium ion increased when the sodium silicate concentration was increased above 40%. Meanwhile, the lithium-ion concentration did not decrease significantly, so the process of separating lithium and magnesium ions became visible. The percentage of lithium-ion loss increased slightly to 77% after the addition of 53% stoichiometric sodium silicate. When sodium silicate was added to the optimum point of 80% stoichiometry, it became 82.26% (Fig 3). The percentage of magnesium ions in sodium silicate above 40% still increased, with the addition of 53% sodium silicate resulting in 92.49% precipitated magnesium ion, and the optimum addition of sodium silicate was 80% magnesium ion precipitated to 99.89% (Fig. 3).

The sodium silicate precipitation process successfully precipitated magnesium ions, according to the experimental results; the optimum results showed that 99.89% of magnesium ions were present in the solid-state, which precipitated into magnesium silicate according to the reaction (1). However, because many lithium ions are bound in solid magnesium silicate as a gel during this precipitation process, lithium ions are removed in the filtrate up to 82.26%. According to a literature review, magnesium silicate is formed by the precipitation of sodium silicate with magnesium ions in the form of a tetrahedral-octahedral gel. The tetrahedral-octahedral gel can bind lithium ions to form a formulation similar to hectorite [21]. This demonstrates that solid magnesium silicate has adsorbed lithium ions, as evidenced by the relatively high percentage of lithium in the filtrate. The lithium-ion concentration in the filtrate is found to be relatively low, at 0.1674 ppm.

3.2 Multi-Stage Process

The single-stage experiment yielded the best results for removing 99.98% magnesium ions and 82.26% lithium ions from the filtrate. The sodium silicate precipitation process, which can reduce the Mg/Li ratio from 10521 to 64, opens the door to the possibility of extracting lithium from seawater.

The six-stage experiment was carried out in reference to the previous single-stage process's optimal condition. The goal of the multi-stage experiment was to reduce lithium ion loss and increase magnesium ion removal in the filtrate, so that the separation of magnesium and lithium ions in the filtrate improved and the Mg/Li ratio decreased. The optimum condition for adding sodium silicate based on the results of the single-stage experiment was 80% stoichiometry or 60 ml of sodium silicate solution. As a result, in a multi-stage experiment, 10 ml of sodium silicate was added to the filtrate per step (6 stages) to ensure that the chemical precipitation process ran smoothly. Previous researchers had never conducted multi-stage experiments in seawater using sodium silicate chemical precipitation techniques. Assume the multi-stage process is effective in significantly reducing lithium ion loss in the filtrate. In that case, further research will be conducted to optimize the multi-stage process.

3.2.1 Ratio Mg/Li in Filtrate after Precipitation

According to the Mg/Li ratio, the multi-stage process yields a higher Mg/Li ratio than the single-stage process. The Mg/li ratio was 64 in the single-stage process and 110 in the multi-stage process. This indicates that the multi-stage process has lower selectivity for magnesium and lithium ions than the single-stage process.

Figure 4 shows that the Mg/li ratio decreases dramatically with each step of the multistage sodium silicate process, from stage 1 (13.33% stoichiometric sodium silicate) to stage 4 (53.33% stoichiometric sodium silicate). The decrease in the Mg/li ratio is very small in the multistage process at stages 5 (66.66% stoichiometric sodium silicate) and 6 (80% stoichiometric sodium silicate). Because the number of magnesium ions in the filtrate is already deficient at stages 4, 5, and 6, only a small amount of magnesium ions can be taken up again with the addition of sodium silicate in the next stage.

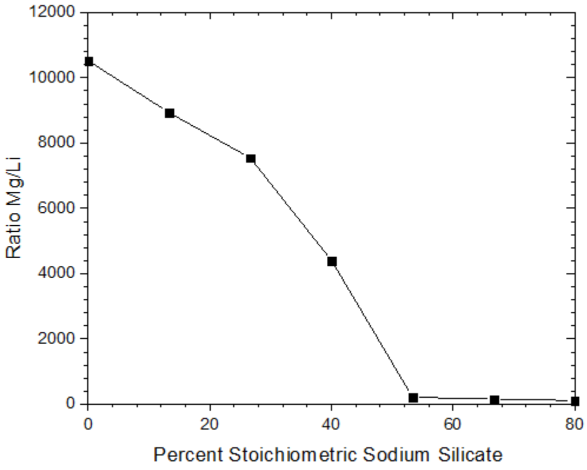

Figure 4. The effect of the addition of sodium silicate on the Mg/Li ratio in the multi-stage sodium silicate precipitation process

When the multi-stage experiment results were compared to the single-stage investigation, the multi-stage process produced a higher Mg/Li ratio than the single-stage process.

3.2.2 The Percentage of Ion Removal in Filtrate after Precipitation (Multi-Stage)

The multistage process in this experiment was carried out in six steps, with each step adding 10 ml of sodium silicate solution, bringing the total to 60 ml (80% stoichiometric). This is based on a single-stage experiment in which the addition of 60 ml of sodium silicate (80% stoichiometric) produced the best results, with the percent lithium-ion loss reaching 82.26% (Fig 2).

The results of the multi-stage experiment showed that the percentage of lithium ions lost increased significantly from the first to fourth stages. The number of lithium ions lost in the fourth stage was 75.41% (Fig 4).

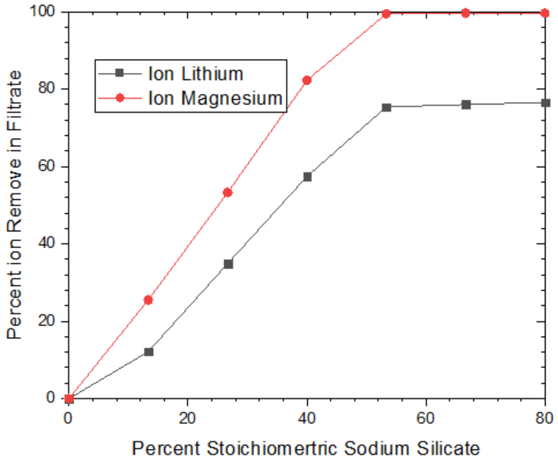

Figure 5. Effect of the addition of sodium silicate on the percentage of ion removal infiltrate in the multi-stage precipitation process

The lithium-ion removal process in the first to fourth stages is also consistent with the magnesium ion precipitation process, in which the precipitated magnesium ion reaches 99.50% purity in the fourth stage (Fig. 5). The experimental results at stages 5 (66.66 percent Stoichiometric Sodium Silicate) and 6 (80 percent Stoichiometric Sodium Silicate) revealed that the percentage of lithium ions reduced in the process fell to 76.54 percent at the end of the precipitation process (Fig 5). When compared to the single-stage process, the multi-stage process reduced lithium-ion removal from 82.26 percent (Fig. 2) to 76.54 percent (Fig. 5). The multi-stage process could only precipitate 99.67 percent magnesium ions (Fig. 5), which was less than the single-stage experiment, which could precipitate up to 99.89% magnesium ions.

Because the results of the multi-stage investigation were slightly better than the single-stage process, it is necessary to develop different process technology to reduce the lithium removal from the filtrate after precipitation.

3.3 The comparison of Associated Elements of Filtrate after Precipitation Process for Single-Stage and Multi-Stage Products

After obtaining the filtrate product from the single-stage and multistage processes, an ICP-OES (inductively coupled plasma-optical emission spectrometry) analysis of the elemental content in the filtrate was performed in the study. This paper compares the element concentrations determined by ICP-OES analysis of the precipitation filtrate to the results of ICP-OES analysis on seawater in Table 1. After learning the results of each element's ICP-OES analysis in seawater and filtrate products in Table 2.

Following the precipitation process, the magnesium content of seawater was determined to be 1761 (Table 1) ppm to 2.08 ppm for the single-stage precipitation process and 4.91 ppm for the multi-stage precipitation process based on the filtrate results.

Tabel 2. Chemical composition of seawater and sodium silicate (ppm)

Element	Single-Stage	Multi-Stage
Magnesium (Mg)	2.08	4.91
Sodium (Na)	4957	5773
Lithium (Li)	0.0324	0.0447
Potassium (K)	148	172
Calcium (Ca)	8	29
Boron (B)	1.98	1.53
Ratio Mg/li	64	110

Because the magnesium content requirement is 173 ppm, the resulting filtrate has the potential to be a lithium carbonate product based on the shallow magnesium content. However, due to the low lithium recovery, processing it into 17,350 ppm lithium concentrate is difficult. According to the literature, the concentrate solution for crystallization of lithium carbonate must contain 17.350 ppm lithium-ion and 173 ppm magnesium ion [22]. The ICP-OES analysis revealed that, with the exception of the element sodium, all ions in the filtrate decreased in concentration after the sodium silicate precipitation process.

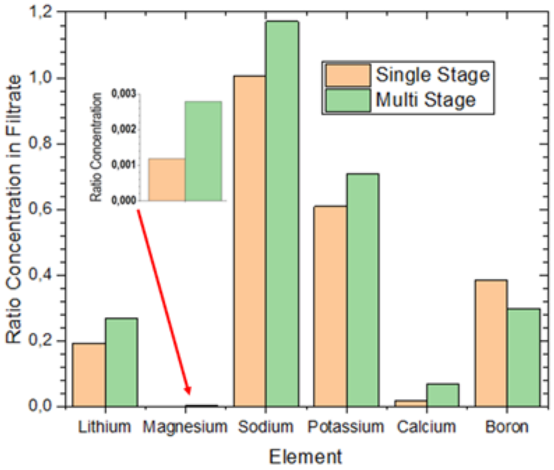

Figure 6. Comparison of the concentration of elements infiltrates after the precipitation process between a single-stage and multi-stages (80 % stoichiometric sodium silicate)

The sodium element in the filtrate product results from sodium silicate precipitation; the sodium content rises due to ion exchange during the precipitation process, particularly magnesium and calcium ions.

The ion analysis results show that the multi-stage process is more profitable, as evidenced by an increase in the content of lithium ions in the filtrates. With the six-stage method, a lithium concentration ratio after precipitation of about 0.267 was obtained in the multi-stage process. In the single-stage experiment, the lithium concentration ratio was 0.193. (Fig. 6). However, the magnesium element increased in the filtrate with the multi-stage methods, rising from a ratio concentration of 0.00118 (single-stage) to 0.00279 (multi-stages) (Fig. 6). The increase in magnesium ions in the filtrate increased the Mg/li ratio from 64 in the single-stage process to 110 in the multi-stages (Fig. 5). According to the experimental results, the technology for extracting lithium concentrate from seawater using the sodium silicate reagent is extremely difficult. Until now, the process of extracting lithium from seawater has been developed using various methods in combination. No industry has been able to economically extract lithium from the sea. Lithium is extracted commercially from brine water with a low Mg/Li ratio all over the world. Salar de Atacama in Chile, for example, has a Mg/Li ratio of 6.4, Salar Del Hombre Muerto in Argentina has a Mg/Li ratio of 1.4, and Silver Peak in the United States has a Mg/Li ratio of 1.4 [14].

3.4 The comparison of Solid Product

3.4.1 Percent Solid after Precipitation

The results of the process with variable sodium silicate addition show that the more sodium silicate added, the more white precipitate is formed. According to the experimental data, the addition of sodium silicate from 13% to 67% stoichiometric shows a significant increase. There was a decrease in the formation of white magnesium silicate precipitate with the addition of between 67% and 80% stoichiometric. Figure 7 shows that the accumulation of 67 percent stoichiometric solids yielded 27.46% and the accumulation of 80% stoichiometric solids yielded 24.25%.

Because 100% stoichiometric sodium silicate with a magnesium ion has not been achieved, there should be no decrease in solids recovery based on the stoichiometric sodium silicate with a magnesium ion addition of between 67% stoichiometric to 80% stoichiometric. Several possibilities exist, including the reaction of sodium silicate and calcium ions to form calcium silicate in the mineral wollastonite [23]. The second possibility is that some magnesium ions become trapped in the gel and do not react with the other sodium silicates.

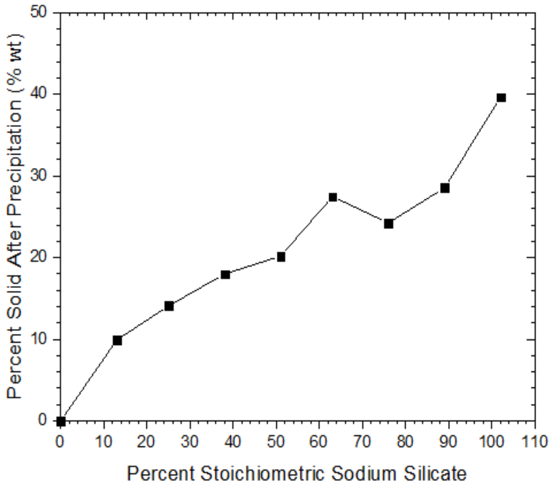

Figure 7. The effect of adding sodium silicate to the single-stage precipitation process on the increase in percent solid

The solids formed in a multi-stage process are similar to those formed in a single-stage process (Fig. 8).

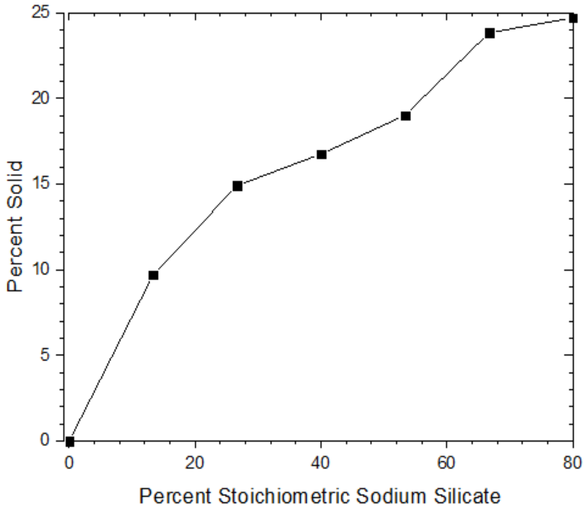

Figure 8. The effect of the addition of sodium silicate on the multi-stage precipitation process on the increase in percent solid

Figure 8 shows that the maximum solid percent formed in the multi-stage process is 24.72%, while in the single-stage process the percent solid obtained is 24.25% (Fig 6). The comparison of multi-stage and single-stage experimental results shows that the single-stage process stores relatively more lithium, magnesium, and other ions than the multi-stage process.

3.4.2 The Phase of Solid Product

XRD (x-ray diffraction) analysis was performed on solids resulting from single-stage and multi-stage precipitation processes.

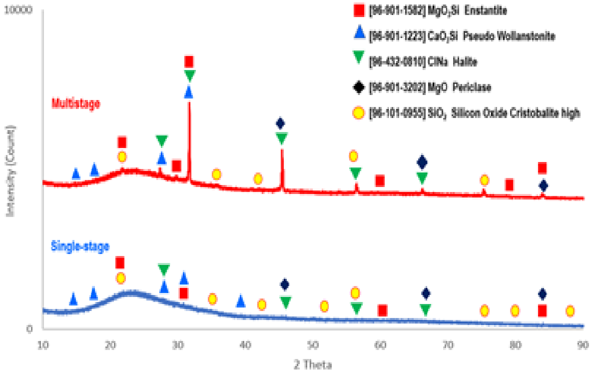

Figure 9. Comparison of XRD analysis results on solid products resulting from sodium silicate precipitation with single-stage and multi-stage processes

XRD analysis revealed that solid magnesium silicate formed peaks at 27.38°, 31.70°, 45.44°, 56.44°, 66.16°, 75.30°, and 83.93° (Fig 9). By looking at the peak point, the analysis carried out with the Match Three program shows five possible compounds with the cations Magnesium, Calcium, Sodium, and Silica. These compounds include Enstantite, Pseudo Wollanstonite, Halite, Periclase, and Cristobalite. Figure 9 shows that the solid form with the single-stage process is still an amorphous compound; in the multistage process it is a crystalline compound with visible peaks. From the results of the Match Three analysis, it can be seen that the composition of the solid compounds.

The results of XRD analysis show that the composition of compounds differs between the single-stage and multi-stage processes, with the single-stage process dominated by silica and the multi-stage process dominated by magnesium silica. In general, the component composition of the solid product is similar to that of talc, with SiO2 content of 59.6% and MgO 19.3% in single-stage production (Table 3).

Tabel 3. Compound arrangement based on Match Three analysis

Compound	Single-Stage	Multi-Stage
[96-901-1582] MgO3Si Enstantite	19.3	81.2
[96-1010955] O2Si Silicon Oxyde Cristobalite	59.6	0.5
[96-901-1223] CaO3Si Pseudo Wollanstonite – 4 A	20.0	6.8
[96-432-0810] Cl Na Halite	0.1	6.4
[96-101-3203] Mg O Periclase	1.1	5.2

From the results of the XRD analysis, it can be seen that the reactions that occur in the precipitation process of sodium silicate and seawater are as follows in the equations below.

$Na_2SiO_3 + Mg^{2+}$ === MgO_3Si (Enstantite) + 2 Na^+…(2)

$Na_2SiO_3 + Mg^{2+}$ === MgO (Periclase) + SiO_2 (Chrystobalite) + 2 Na^+ …(3)

$Na_2SiO_3 + Ca^{2+}$ === CaO_3Si (Pseudo Wollanstonite) + 2 Na^+ …(4)

Talc compounds found in Turkey have a chemical structure of $Mg_3(Si_2O_5)_2(OH)_2$. Theoretically, it has a chemical composition of 63.5 wt.% of SiO_2, and 31.7 wt.% of MgO, and 4.8 wt.% of H_2O [24]. From the results of solids characterization, it can be seen that there is a possibility that the solids can be used as raw material for synthetic talc.

4. CONCLUSIONS

The goal of this experiment is to separate magnesium ions from seawater in order to liberate a lithium solution from magnesium ions. The precipitation experiment results revealed that the addition of 80 percent stoichiometric sodium silicate resulted in the most effective separation of lithium and magnesium ions. The Mg/Li ratio in the filtrate was reduced from 10521 before precipitation to 64 after precipitation, which was the most effective result. When lithium and magnesium ions are separated using the sodium silicate precipitation process, the removed lithium from the filtrate is 82,26%. The multi-stage process could only reduce the amount of lithium-ion lost in the filtrate from 82.26% to 76.54%. According to the findings of this study, the sodium silicate precipitation process was ineffective in separating lithium and magnesium ions from seawater in both single-stage and multi-stage processes. Because the obtained solids have a chemical structure similar to talc, solid products could be used as basic ingredients in the pharmaceutical industry.

ACKNOWLEDGMENT

Thank you to the National Research and Innovation Agency's Research Center for Metallurgy for supporting the activities of the Red and White Lithium Battery, the national research priority grant in 2021.

REFERENCES

[1] P. Loganathan, G. Naidu, and S. Vigneswaran, "Mining valuable minerals from seawater: A critical review,"

Environmental Science: Water Research and Technology, vol. 3, no. 1, pp. 37-53, 2017. Doi: 10.1039/c6ew00268d.

[2] S. Yang, F. Zhang, H. Ding, P. He, and H. Zhou, "Lithium Metal Extraction from Seawater", *Joule*, vol. 2, pp. 1648-1651, 2018. Doi : 10.1016/j.joule.2018.07.006.

[3] S. Murodjon, X. Yu, M. Li, J. Duo, and T. Deng, "Lithium recovery from brines including seawater, salt lake brine, underground water, and geothermal water," *Thermodynamics and Energy Engineering*, pp. 1-39, 2020. Doi: 10.5772/intechopen.90371.

[4] L. Liu, H. Zhang, Y. Zhang, D. Cao, and X. Zhao, "Lithium extraction from seawater by manganese oxide ion sieve MnO2·0.5H2O," *Colloids and Surfaces A: Physicochemical and Engineering Aspects*, vol. 468, pp. 280-284, 2015. Doi: 10.1016/j.colsurfa.2014.12.025.

[5] T. Ryu, Y. Haldorai, A. Rengaraj, J. Shin, H. J. Hong, G. W. Lee, Y. K. Han, Y. S. Huh, and K. S. Chung, "Recovery of lithium ions from seawater using a continuous flow adsorption column packed with granulated chitosan-lithium manganese oxide," *Industrial and Engineering Chemistry Research*, vol. 55, no. 26, pp. 7218-7225, 2016. Doi: 10.1021/ acs.iecr.6b01632.

[6] F. Yang, S. Chen, C. Shi, F. Xue, X. Zhang, S. Ju, and W. Xing, "A facile synthesis of hexagonal spinel λ-MnO2 ion-sieves for highly selective Li+ adsorption," *Processes*, vol. 6, no. 5, 2018. Doi: 10.3390/pr6050059.

[7] Z. Li, C. Li, X. Liu, L. Cao, P. Li, R. Wei, X. Li, D. Guo, K. W. Huang, and Z. Lai, "Continuous electrical pumping membrane process for seawater lithium mining," *Energy and Environmental Science*, vol. 14, no. 5, pp. 3152-3159, 2021. Doi: 10.1039/d1ee00354b.

[8] C. Liu, Y. Li, D. Lin, P. C. Hsu, B. Liu, G. Yan, T. Wu, Y. Cui, and S. Chu, "Lithium extraction from seawater through pulsed electrochemical intercalation," *Joule*, vol. 4, no. 7, pp. 1459-1469, 2020. Doi: 10.1016/j.joule.2020.05.017.

[9] N. Um and T. Hirato, "Precipitation behavior of $Ca(OH)_2$, $Mg(OH)_2$, and $Mn(OH)_2$ from $CaCl_2$, $MgCl_2$, and $MnCl_2$ in NaOH-H_2O solutions and study of lithium recovery from seawater via two-stage precipitation process," *Hydrometallurgy*, vol. 146, pp. 142-148, 2014. Doi: 10.1016/j. hydromet. 2014. 04.006.

[10] T. Takeuchi, "Extraction of lithium from seawater with metallic aluminum," *Journal of Nuclear Science and Technology*, vol. 17, no. 12, pp. 922-928, 1980. Doi: 10.1080/18811248.1980. 9732675.

[11] M. Apriani, W. Hadi, and A. Masduqi, "Physicochemical properties of seawater and bittern in Indonesia: Quality improvement and potential resources utilization for marine environmental sustainability," *Journal of Ecological Engineering*, vol. 19, no. 3, pp. 1-10, 2018. Doi: 10.12911/22998993/86150.

[12] E. Sulistiyono, S. Harjanto, and L. H. Lalasari, "Extraction of magnesium from salt pond waste with low lithium grade using sodium silicate reagent," *IOP Conference Series: Materials Science and Engineering*, vol. 1195, no. 1, pp. 012028, 2021. Doi: 10.1088/1757-899x/1195/1/012028.

[13] H. Vikström, S. Davidsson, and M. Höök, "Lithium availability and future production outlooks," *Applied Energy*, vol. 110, pp. 252-266, 2013. Doi: 10.1016/j.apenergy. 2013. 04.005.

[14] Y. Zhang, Y. Hu, L. Wang, and W. Sun, "Systematic review of lithium extraction from salt-lake brines via precipitation approaches," *Minerals Engineering*, vol. 139, pp. 105868, 2019. Doi: 10.1016/ j.mineng.2019.105868.

[15] X. Liu, M. Zhong, X. Chen, J. Li, L. He, and Z. Zhao, "Enriching lithium and separating lithium to magnesium from sulfate type salt lake brine," *Hydrometallurgy*, vol. 192, pp. 105247, 2020. Doi: 10.1016/j.hydromet.2020.105247.

[16] E. Sulistiyono, L. H. Lalasari, W. Mayangsari, and A. B. Prasetyo, "Study of lithium extraction from brine water, Bledug Kuwu, Indonesia by the precipitation series of oxalic acid and carbonate sodium," *AIP Conference Proceedings*, vol. 1964, 2018. Doi: 10.1063/1.5038289.

[17] L. He, W. Xu, Y. Song, X. Liu, and Z. Zhao, "Selective removal of magnesium from a lithium-concentrated anolyte by magnesium ammonium phosphate precipitation," *Separation and Purification Technology*, vol. 187, pp. 214-220, 2017. Doi: 10.1016/j.seppur.2017.04.028.

[18] Y. Zhang, Y. Hu, N. Sun, S. A. Khoso, L. Wang, and W. Sun, "A novel precipitant for separating lithium from magnesium in high Mg/Li ratio brine," *Hydrometallurgy*, vol. 187, pp. 125-133, 2019. Doi: 10.1016/j.hydromet.2019.05.019.

[19] M. Claverie, A. Dumas, C. Careme, M. Poirier, C. L. Roux, P. Micoud, F. Martin, and C. Aymonier , "Synthetic talc and talc-like structures: Preparation, features, and applications," *Chemistry-A European Journal*, vol. 24, no. 3, pp. 519-542, 2018. Doi: 10.1002/chem.201702763.

[20] A. Kunzmann, Z. Arifin, and G. Baum, "Pollution of coastal areas of jakarta bay: Water quality and biological responses," *Marine Research in Indonesia*, vol. 43, no. 1, pp. 37-51, 2018. Doi: 0.14203/mri.v43i1.299.

[21] C. Hai, Y. Zhou, M. Fuji, T. Shirai, X. Rena, J. Zenga, X. Lia, "Electrical conductivity of hydrothermally synthesized sodium lithium magnesium silicate," *Materials Research Bulletin*, vol. 97, pp. 473-482, 2018. Doi: 10.1016 /j.materresbull. 2017.09.048.

[22] N. Linneen, R. Bhave, and D. Woerner, "Purification of industrial-grade lithium chloride for the recovery of high purity battery-grade lithium carbonate," *Separation and Purification Technology*, pp. 168-173, 2019. Doi: 10.1016/j.seppur. 2018. 05. 020.

[23] G. M. Azarov, E. v. Maiorova, M. A. Oborina, and A. v. Belyakov, "Wollastonite raw materials and their applications (a review)," *Glass and Ceramics*, vol. 52, no. 9. pp. 237-240, 1995. Doi: 10.1007 / BF00681090.

[24] E. Bahri, S. Dikmen, A. Yildiz, R. Gören, and Ö. Elitok, " Mineralogical and physicochemical properties of talc from Emirdağ, Afyonkarahisar, Turkey," *Turkish Journal of Earth Sciences*, vol. 22, no. 4, pp. 632-644, 2013. Doi: 10.3906/yer-1112-14.

Metalurgi (2022) 1: 31 - 38

BRIN
BADAN RISET
DAN INOVASI NASIONAL

METALURGI
Majalah Ilmu dan Teknologi
p-ISSN 0126-3188 | e-ISSN 2443-3926
ejurnalmaterialmetalurgi.lipi.go.id

THE EFFECT OF VOLTSAGE AND TIME IN SYNTHESIS OF MANGANESE DIOXIDE FROM MANGANESE SULFATE PRECURSOR

Eka Fitri Wulandari[a-*], Lia Andriyah[b], Soesaptri Oediyani[a], Latifa Hanum Lalasari[b], Tri Arini[b], Nadia Crisayu Natasha[b], Fariza Eka Yunita[b], Ariyo Suharyanto[b], Eko Sulistiyono[b]
[a]Departemen Teknik Metalurgi, Universitas Sultan Ageng Tirtayasa
Jl. Jenderal Sudirman Km 3, Cilegon, Banten, Indonesia, 42435
[b] Pusat Penelitian Metalurgi dan Material
Gedung 470, Kawasan Puspiptek Serpong, Banten, Indonesia, 15343
*E-mail: fitrieka29@gmail.com

Received : 16-08-2021, Revised : 02-06-2022, Accepted : 23-06-2022

Abstract

The utilization of manganese dioxide (MnO_2) as a cathode material for lithium-ion batteries has attracted considerable attention due to its high theoretical storage capacity of 615 mAh/g. In this study, the synthesis of MnO_2 was carried out from manganese sulfate ($MnSO_4$) precursor, a pregnant solution from the leaching process of manganese ore from Trenggalek Regency. The electrolysis method has been used in this synthesis of MnO_2 in an electrochemical cell consisting of two graphite electrodes with dimensions of (16 x 5 x 0.3) cm. The purpose of this study is to determine the effect of voltsage and time on particles produced of MnO_2, the phase and crystal structure by MnO_2, and its morphological microstructure. The electrolysis process was carried out in 2,000 ml of $MnSO_4$ solution under constant stirring at 60 °C with DC voltsage varied by 2, 4, 6, and 8 volts and time run by 4, 8, 12, and 16 hours. The precipitates formed at the anode were separated, then the particles were dried at 110°C for 2 hours. The composition of MnO_2 was analyzed by XRF (x-ray fluorescence), the phase and crystal structure were evaluated by XRD (x-ray diffraction), and the morphological microstructure was captured by SEM (scanning electron microscope). The results revealed that the highest mass gain of MnO_2 produced is 31.63 grams which are electrolyzed at 8 voltss for 16 hours. The highest purity of MnO_2 is 89.23% which is electrolyzed at 2 voltss for 16 hours. The particles produced were α-MnO_2 with a tetragonal crystal system and nearly spherical with size particles ranging from 136.01-202.48 and 144-352 nm.

Keywords: *Manganese sulfate, manganese dioxide, electrolysis, crystal structure, polymorphy*

1. INTRODUCTION

Manganese mineral is one of Indonesia's natural resources. The manganese mineral occurs in nature commonly as pyrolusite (MnO_2) and psilomelane ($BaH_2O_2.Mn_5O_{10}$). According to the United States Geological Survey (USGS), about 85-90% of manganese use in the world is applied to the metallurgical industry. In comparison the remaining 10% is applied to the non-metallurgical industry. According to the Geological Agency, in 2015, Indonesia had 61,631,820 tons of manganese ore resources and 87,236,536 tons of manganese ore reserves spread across several regions in Indonesia [1]. Trenggalek Regency in East Java Province has one the best quality of manganese ores [2].

Manganese ore in Trenggalek Regency is found as pyrolusite with a Grade A quality that contains above 40% MnO_2 [3]-[4]. The compositions of manganese ore from the Trenggalek Regency are shown in Table 1, which shows that the MnO_2 level in manganese ore from Trenggalek Regency is about 46.03% [5]. However, the manganese ore from Trenggalek Regency has not been used optimally [2],[4]. Therefore, further research is needed to get the desired product, especially

DOI : 10.14203/metalurgi.v37i1.599

Metalurgi is Sinta 2 Journal (https://sinta.ristekbrin.go.id/journals/detail?id=3708) accredited by Ministry of Research & Technology, Republic of Indonesia

using MnO_2 as cathode material for lithium-ion batteries.

Table 1. XRF analysis results of manganese ore from Trenggalek Regency [5]

Compounds	Wt. %
Manganese (MnO_2)	46.03
Silica (SiO_2)	48.73
Iron Oxide (Fe_2O_3)	3.77
Calcium (CaO)	1.10
Barium (BaO)	0.46
Phosphor (P_2O_5)	0.56

Lithium-ion batteries have been widely developed because of their advantages; a high energy efficiency of about 75-90%, long cycle life of about 500-2000 cycles, and low self-discharge of about 5-10% per month [6]. Cobalt has been commonly used in commercial lithium-ion batteries, known as LCO (lithium cobalt oxide). However, the development of LCOs is hampered due to their high cost and environmental issues, which are considered unfriendly to the environment [7]. Various oxides of transition metals have been studied as alternative cathode materials for lithium-ion batteries. From the different transition metal oxide, manganese dioxide (MnO_2) has attracted so much attention to be used as a cathode material for lithium-ion batteries due to its high storage capacity of 615 mAh/g [8], which is expected to fulfill the demands of high performance of lithium-ion batteries. Manganese dioxide is also considered to have the potential to be used as a lithium-ion battery cathode because of its abundant natural resources [9].

Manganese dioxide has various polymorphic crystal structures, including β-, α-, δ-, and γ-MnO_2. The electrochemical properties of manganese dioxide depend on the crystal structure and morphology of the oxide. From the various polymorphic crystal structures of manganese dioxide, α-MnO_2 has special attention as a cathode material for lithium-ion batteries due to the presence of a 2x2 tunnel in its crystal lattice, which is considered to facilitate accommodation and transport for the inclusion of lithium ions [10].

MnO_2 particles can be prepared by the electrolysis method. The electrolysis method was chosen in this study due to its uncomplicated process compared with hydrothermal, sol-gel, sonochemical, and other methods. Widiyastuti et al., [11] reported that α-MnO_2 had been successfully prepared from the $KmnO_4$ solution by electrolysis method using two carbon electrodes with 2 voltss applied. The particles were rod-like in shape with a diameter of 493.22 nm. In this study, the synthesis of MnO_2 by electrolysis method will be developed from manganese sulfate ($MnSO_4$) precursor, which is a pregnant leach solution from the leaching process of manganese ore from Trenggalek Regency. The Electrolysis process was carried out with variations of voltsage and time to determine its effect on the mass gain of obtained MnO_2 and to determine the polymorphic crystal structure and the morphology of obtained MnO_2.

2. MATERIALS AND METHODS

A pregnant leach solution of manganese sulfate ($MnSO_4$) produced by the leaching process of manganese ore from Trenggalek Regency was used as a precursor in this study. This process was carried out in an electrochemical cell consisting of two graphite electrodes with dimensions of (16 x 5 x 0.3) cm. The schematic of the electrolytic cell is shown in Fig.1. The electrodes were set in parallel with the anode connected to (+) and the cathode connected to (-) polar of the DC power supply. The distance between anode and cathode was 5 cm, and both anode and cathode were immersed into $MnSO_4$ solution with a final depth of 8 cm.

The sample was first filtered and then analyzed by ICP-OES (inductively couple plasma-optical emission spectroscopy) to determine the compositions of $MnSO_4$ solution before being processed by the electrolysis method. The electrolysis process was carried out in 2000 ml of $MnSO_4$ solution under constant stirring at 60ºC with DC voltsage varied by 2, 4, 6, and 8 voltss and time varied by 4, 8, 12, and 16 hours. The precipitates formed at the anode were separated, then the particles were dried at 110 °C for 2 hours to get a powder of MnO_2. At the end of the experiment, the product was weighed to determine the mass gain of obtained MnO_2.

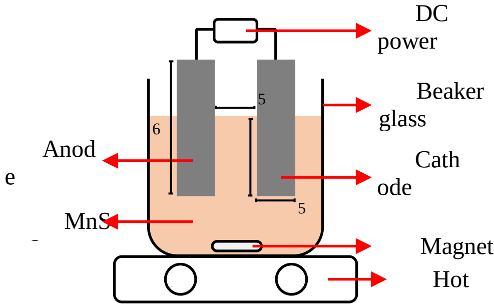

Figure 1. The schematic of electrolytic cells

The compositions of MnO_2 were then analyzed by XRF (x-ray fluorescence), the phase and crystal structure were also evaluated by XRD (x-ray diffraction), and the morphological microstructure was captured by SEM (scanning electron microscope) for further analysis.

3. RESULT AND DISCUSSION

The ICP-OES (inductively couple plasma-optical emission spectroscopy) results of $MnSO_4$ solution before processed by electrolysis method are shown in Table 2 which shows that the manganese (Mn) level in $MnSO_4$ solution is 384.033 ppm.

Table 2. $MnSO_4$ initial composition analyzed by ICP-OES

Element	ppm	Element	ppm
Ag	0.01178	Fe	0.05516
Al	0.36621	K	0.05516
Ca	3.32535	Mg	1.02671
Co	0.03355	Mn	384.033
Cr	0.08665	Na	0.99584
Cu	0.21774	Ni	0.07297

In a synthesis of MnO_2 prepared by the electrolysis method, electrical energy is converted directly into chemical energy, which is stored in the products of the reaction. When the current is passed through the $MnSO_4$ solution, the reaction will occur as an anodic and cathodic reaction. The anodic reaction would be processed in three steps, as shown in Equations (1)-(3). The cathodic reaction and the overall reaction can be written as shown in Equation (4)-(5) [12]. During the reaction, manganese is deposited at the anode as MnO_2.

$$Mn^{2+} + 2H_2O \rightleftharpoons MnO_2 + 4H^+ + 2e^- \quad (1)$$
$$MnO_2 + Mn^{2+} + 2H_2O \rightleftharpoons 2MnOOH + 2H^+ \quad (2)$$
$$MnOOH \rightleftharpoons MnO_2 + H^+ + e^- \quad (3)$$
$$2H^+ + 2e^- \rightleftharpoons H_2 \quad (4)$$
$$MnSO_4 + 2H_2O \rightleftharpoons MnO_2 + H_2SO_4 + H_2 \quad (5)$$

The color transformation of MnSO4 solution can observe the synthesis of MnO_2. The color of $MnSO_4$ was pink before electrolysis; and then it turned black. It happens due to the decreasing Mn content in $MnSO_4$ solution during the electrolysis process. The most significant color transformation of $MnSO_4$ is in a condition of 8 voltss applied for 16 hours, as shown in Fig. 2. During the electrolysis process, bubbles are also formed at cathode due to the hydrogen that occurs in cathodic reaction as written in Equation 4.


(a) (b)

Figure 2. MnSO4 solution processed by electrolysis method: (a) before processed, (b) after processed

$MnSO_4$ solutions were then analyzed again by ICP-OES to determine the compositions of $MnSO_4$ after being prepared by electrolysis. The ICP-OES results of $MnSO_4$ are shown in Table 3, which indicates that the Mn level in $MnSO_4$ is 142.232 ppm.

Table 3. ICP-OES analysis results of $MnSO_4$ solution after processed by electrolysis method at 2 volts for 16 hours

Element	ppm	Element	ppm
Ag	0.15151	Fe	0.40623
Al	0.59212	K	0.63093
Ca	3.24400	Mg	0.96942
Co	0.03123	Mn	142.232
Cr	0.16532	Na	1.41810
Cu	0.14877	Ni	0.12794

It decreases due to reactions during the electrolysis process, which transform the Mn to MnO_2 deposited, and it also causes the increasing of other elements in solution.

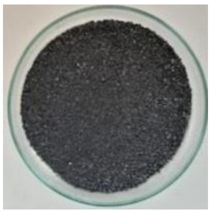

Figure 3. Manganese dioxide prepared by electrolysis method

The precipitates formed at anode were separated, then the particles were dried to get a powder of MnO_2. The obtained MnO_2 prepared by electrolysis is a solid black as shown in Fig. 3.

3.1 Synthesis of MnO_2 in Various Voltsage Prepared by Electrolysis

The electrolysis process was carried out with various voltsages applied by 2, 4, 6, and 8 voltss. The effect of voltsage on the mass gain of MnO_2 produced by electrolysis is shown in Fig. 4. It is expected that increasing the voltsage of electrolysis will lead to an increased mass gain of MnO_2.

According to the results, the mass gain of MnO_2 produced by the electrolysis method is directly proportional to the voltsage applied.

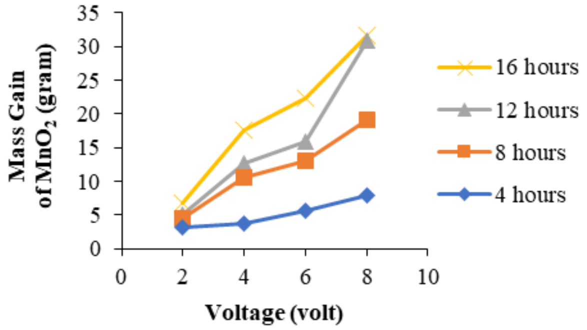

Figure 4. The effect of voltsage on mass gain of MnO_2 prepared by electrolysis

The voltsage used in electrolysis will affect the amount of current, as written in Equation 6.

$$V = i \times r \qquad (6)$$

V is voltsage in volts (V), *i* is current in ampere (A), and *r* is resistance in ohm. The higher voltsage will increase the amount of current passing through the electrolyte, which will also lead to a rise in the rate of particles produced at the anode. It has been well-known, as stated in Faraday's law, that the amount of particles produced is directly proportional to the current passing through the electrolyte, which is written in Equation 7.

$$W = \frac{e \times i \times t}{F} \qquad (7)$$

Where *w* is the mass of species produced at the electrode in gram (g), *e* is equivalent weight in gram/mol, I is the current in ampere (A), and F is Faraday constant which is equal to 96,500 coulombs. 1F is the charge required to dissolve 1g equivalent of the anode.

3.2 Synthesis of MnO_2 in Various Time Prepared by Electrolysis

The electrolysis process was carried out with time varied by 4, 8, 12, and 16 hours. As shown in Fig. 5, the mass gain of MnO_2 produced increases during electrolysis for a longer time. The highest mass gain of MnO_2 is prepared for 16 hours, and the lowest is prepared for 4 hours. It is expected that increasing the time of electrolysis will lead to an increased amount of particles produced.

According to the results, the mass gain of MnO_2 produced by the electrolysis process is directly proportional to the electrolysis time. The longer time of electrolysis will lead to an increase in the rate of particles produced at the anode, and therefore, it will also increase the mass gain of MnO_2. As stated in Faraday's law, it is also suitable that the amount of particles produced in the electrolysis process is directly proportional to the electrolysis time, as written in Equation 7.

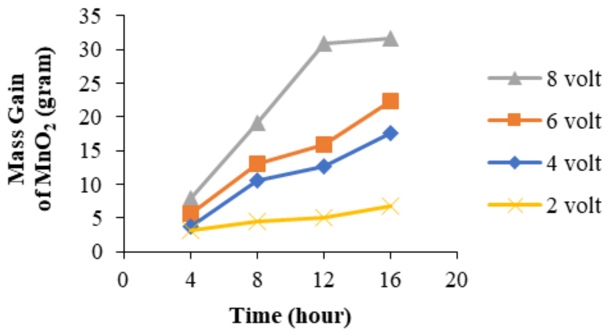

Figure 5. The effect of time on mass gain of MnO_2 prepared by electrolysis

This result is also similar to the previous study, Hidayat et al., [13] reported that electrolysis of MnO_2 from battery waste produces 0.0341 gram MnO_2 at 20 minutes and 0.1045 gram at 60 minutes. Both were electrolyzed at 5 voltss. It means that increasing the time of electrolysis will also increase the mass gain of MnO_2.

3.3 XRF Analysis Results

The compositions of obtained MnO_2 were analyzed by XRF (x-ray fluorescence). The XRF characterization was done on MnO_2 particles prepared at 2 voltss for 16 hours.

Table 4. XRF results of MnO_2 particles prepared by electrolysis at 2 volts for 16 hours

Compounds	%	Compounds	%
K_2O	0.118	NiO	0
MoO_3	0.026	SO_3	1.025
TiO_2	0.014	SiO_2	6.664
MnO_2	89.231	CaO	0.148
Fe_2O_3	2.567	Cr_2O_3	0.155
V_2O_5	0.050		

According to the results, in Table 4, the level of MnO_2 is 89.231%. It indicates that the electrolysis process can potentially increase the MnO_2 level.

The lower MnO_2 level indicated that the impurity level in MnO_2 is still relatively high, and it will decrease the performance of MnO_2 as a cathode material for lithium-ion batteries. Therefore, MnO_2 needed for producing lithium-ion batteries must have high purity. According to the Ministry of Energy and Mineral Resources Republic of Indonesia No. 25 the year 2018, the minimum purity of MnO_2 processed by the electrolysis method is 90% [14], which has not been achieved in this study of synthesis of MnO_2.

3.4 XRD Analysis Results

The polymorphic crystal structure of obtained MnO_2 was analyzed by XRD (x-ray diffraction). The XRD characterization was done to particles of MnO_2 prepared with various voltsages applied by 2, 4, 6, and 8 voltss for 16 hours. The XRD patterns of MnO_2 particles prepared with multiple conditions are shown in Figure 6. The XRD patterns for all samples are compared to the ICDD (*international center for diffraction data*) database using the PANalytical HighScore Plus application to determine the polymorphic crystal structure. As shown in Figure 6, all the diffraction peaks of particles are in good agreement with ICCD database No. 00-044-0141, which is the standard value of α-MnO_2. According to ICDD database No. 00-044-014, α-MnO_2 has a tetragonal crystal system.

The electrochemical properties of MnO_2 strongly depend on its crystal structure and morphology of the oxide. As stated by Yang et al., [10], α-MnO_2 has the greatest electrochemical properties of other forms due to the presence of a 2x2 tunnel in its crystal lattice, affecting its storage capacity. Therefore, it's great to be used as cathode material for lithium-ion batteries since they require a high storage capacity.

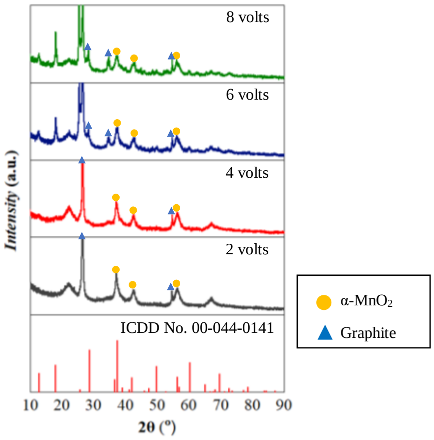

Figure 6. XRD pattern of MnO_2 particles prepared by electrolysis at various voltsages for 16 hours compared to ICDD data base No. 00-044-0141

The patterns for all samples have five characteristic peaks at 2θ= 37°, 42°, 56° which matches with the value of α-MnO_2. However, there are also other peaks which match with the ICDD No. 96-900-0047 database that belongs to graphite. Graphite is an inert electrode, but also a very brittle compound due to its perpendicular planes. Therefore, the existence of graphite in XRD patterns for all samples is expected to come from the electrodes when the deposits at the anode were being separated since graphite is a very brittle compound. As shown in Figure 6, the peaks that belong to impurity increased along with the higher voltsage. It also shows that all the XRD patterns have a different intensity which is the higher intensity is found in the XRD pattern of MnO_2 prepared at 2 voltss for 16 hours, and the lowest one found in the XRD pattern of MnO_2 prepared with 8 voltss applied for 16 hours.

According to the results, the XRD patterns do not exhibit well-defined peaks along with the higher voltsage. Nursiti et al., [15] and Widiyastuti et al., [11] also reported the same result in a previous study of synthesis of MnO_2 prepared by electrolysis from $KMnO_4$ solution; both said that the XRD patterns exhibit well-defined peaks at particles prepared at the lower voltsage. It indicated a poor crystalline of these materials. Increasing the voltsage only lead to increasing the production rate of MnO_2 particles as it has been known that the amount of particles deposited at electrodes in the electrolysis process is directly proportional to the current as stated in Faraday's law. The current, in this case, is also directly proportional to the voltsage.

3.5 SEM Analysis Results

The morphology of obtained MnO_2 was analyzed by SEM (*scanning electron microscope*). The SEM characterization was done to obtain MnO_2 with the highest purity of MnO_2, which is electrolyzed at 2 voltss for 16 hours, and the lowest one, which is electrolyzed at 8 voltss for 16 hours to see the difference. The SEM results of obtained MnO_2 with 2 volts voltsage applied are shown in Fig. 7. At a magnification of 5,000x, it is clearly shown that the particles are not agglomerated. However, the morphology of particles is slightly difficult to be observed. The image likely indicates that the particles may have a nearly spherical morphology. At a magnification of 20,000x, as shown in Fig. 7(b), the particles of MnO_2 have a size ranging from 136.01-202.48 nm.

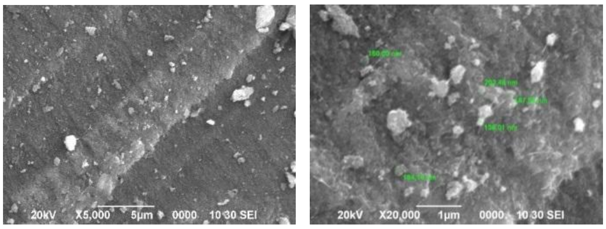

(a) (b)

Figure 7. SEM image of MnO_2 particles prepared by electrolysis method with 2 volts applied for 16 hours at (a) magnification of 5,000x and (b) magnification of 20,000x

The SEM results of obtained MnO_2 with 2 volts applied for 16 hours are shown in Figure 8. At a magnification of 5,000x, the particles appear as many agglomerates of very nearly spherical. On the other hand, at a magnification of 20,000x as shown in Fig. 8(b), it shows that the particles have a nearly spherical shape morphology with a size ranging from 144-352 nm. According to the results, it is clearly shown that the particles of MnO_2 prepared with 2 volts applied to have a smaller particle size compared to the particle size of MnO_2 equipped with 8 volts applied. This result is similar to the previous study, Viscarini et al., [16] have been reported that the particles prepared by electrolysis of $KMnO_4$ solution at 2 volts have a larger particle size area than the particles prepared at the higher voltage. According to the results, it can be noted that increasing the voltage during electrolysis, in this case, will also increase the particle size of obtained MnO_2. The particle size of obtained MnO_2 will also influence the quality of MnO_2 as cathode material for lithium-ion batteries; the smaller particle size makes a surface area more prominent. A larger surface area will also make the storage capacity of MnO_2 become larger. Therefore, it improves the quality of MnO_2 as cathode material for lithium-ion batteries.

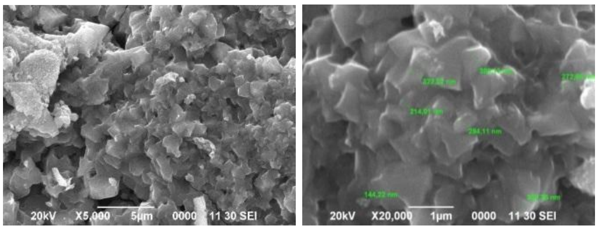

(a) (b)

Figure 8. SEM image of MnO_2 particles prepared by electrolysis method with 8 volts applied for 16 hours at (a) magnification of 5,000x and (b) magnification of 20,000x

4. CONCLUSION

Manganese dioxide has been successfully prepared at various voltage and times by electrolysis of $MnSO_4$ using two graphite electrodes. The highest amount of obtained MnO_2 is 31.63 grams which are electrolyzed at 8 volts for 16 hours. The highest purity of obtained MnO_2 is 89.23% which is electrolyzed at 2 volts for 16 hours. The particles have nearly spherical shape morphology with size ranging from 136.01-202.48 nm which is electrolyzed at 2 volts for 16 hours and 144-352 nm which is electrolyzed at 8 volts for 16 hours. The particles produced were α-MnO_2 with a tetragonal crystal system.

ACKNOWLEDGMENT

The authors would like to thank the Research Center of Metallurgy BRIN for the facilities and funding, as well as the researchers and staff who contributed significantly to this study.

REFERENCES

[1] ESDM, “BAB I”, in Kajian dampak hilirisasi mineral mangan terhadap perekonomian regional, bab I, pp. 1-2, 2017.

[2] A. Royani, E. Sulistiyono, L. Andriyah, “Studi pelarutan mangan sulfat sebagai bahan sel baterai litium manganese,” *Prosiding Teknologi untuk Mendukung Pembangunan Nasional*, pp. 64-67, 2013.

[3] I. Sukandarrumidi, “Bab 5: Bahan galian industri yang berkaitan dengan batuan sedimen, sub bab: mangan” in *Bahan Galian Industri*," Yogyakarta: Gadjah Mada University Press, pp. 95-103, 1999.

[4] D. Yuliatin, "Potensi mangan di Gunung Kuncung Kecamatan Pogalan Kabupaten Trenggalek," Blora: PTK AKAMIGAS-STEM, pp. 5-6, 2013.

[5] L. Andriyah and E. Sulistiyono, “Proses permurnian mangan sulfat dengan pengendapan selektif menggunakan karbon aktif dan larutan NaOH,” Technical Report, pp. 2, 2014.

[6] A. Biswal, B. C. Tripathy, K. Sanjay, T. Subbaiah, and M. Minakshi, “Electrolytic manganese dioxide (EMD): A perspective on worldwide production, reserves and its role in electrochemistry,” *RSC Adv.*, vol. 5, no. 72, pp. 58255-58283, 2015. Doi: 10.1039/c5ra05892a.

[7] A. Royani, “Pembuatan serbuk mangan sulfat dari pelindian bijih mangan kadar rendah dengan metode kristalisasi,” *JTERA (Jurnal Teknologi Rekayasa)*, vol. 4, no. 1, pp. 53-60, 2019. Doi: 10.31544/jtera.v4.i1.2019.53-60.

[8] L. Xing, C. Cui, C. Ma, and X. Xue, “Facile synthesis of α-MnO_2/graphene nanocomposites and their high performance as lithium-ion battery anode”. *Mater. Lett.*, vol. 65, no. 14, pp. 2104-2106, 2011. Doi: 10.1016/j.matlet.2011.04.093.

[9] M.-M. Zou, D.-J. Ai, and K.-Y. Liu, “Template synthesis of MnO_2/CNT nanocomposite and its application In rechargeable lithium batteries,” *Trans. Nonferrous Met. Soc. China*, vol. 21, no. 9, pp. 2010-2014, 2011. Doi: 10.1016/s1003-6326(11)60964-3.

[10] Y. Yang, L. Xiao, Y. Zhao, and F. Wang, “Hydrothermal synthesis and

electrochemical characterization of α-MnO_2 nanorods as cathode material for lithium batteries," *Int. J. Electrochem. Sci.*, vol. 3, no. 1, pp. 67-74, 2008. Doi: 10.20964/2022.07.36.

[11] W. Widiyastuti, P. Nurlilasari, S. Affandi, and H. Setiawan, "Electrolysis synthesis of MnO_2 in acidic environment and its electrochemical performance for supercapacitor," *JPhCS*, vol. 1093, no. 1, pp. 12021, 2018. Doi: 10.1088/1742-6596/1093/1/012021.

[12] M. Sugimori and T. Sekine, "Denki kagaku oyobi kagyo," *Butsuri Kagaku*, vol. 37, pp. 63, 1969.

[13] Hidayat, M. I, "Pemisahan mangan dioksida (MnO_2) dari limbah pasta baterai dengan metode elektrolisis," Doctoral Dissertation, Institut Teknologi Sepuluh Nopember, pp. 38-39, 2017. Doi: 10.12962/j23373520.v6i2.27786

[14] Dinas Energi dan Sumber Daya Mineral, "Himpunan peraturan perundangan di bidang energi dan sumber daya mineral," vol. 6, no. 2, pp. 233, 2019.

[15] Nursiti, E. R. Wibowo, A. W. Safitri, Supriyono, and R. Oktaviani, "Electrosynthesis of α-MnO_2/C nanocomposite and it's fabrication for supercapacitor application," *Jurnal Chemugury*, vol. 02, no. 1, pp. 6-11, 2018. Doi: 10.30872/cmg.v2i1.1631.

[16] V. P. Viscarini and N. U. R. Rokhima, "BAB IV" in Sintesa partikel MnO_2 dengan teknik elektrokimia dalam sel membran, Surabaya: Institut Teknologi Sepuluh Nopember, pp. 16-21, 2015.

AUTHOR INDEX

A
Aditianto Ramelan, 7
Ariyo Suharyanto, 31
Aristo Nugraha Putra, 1

B
Budi Hartono Setiamarga, 1

C
Cherly Selindiana, 7

E
Eddy Sumarno Siradj, 15
Efendi Mabruri, 15
Eka Fitri Wulandari, 31
Eko Sulistiyono, 21; 31
Erie Martides, 15

F
Fariza Eka Yunita, 31
Florentinus Firdiyono, 21
Francoise Lantang, 1

H
Hermawan Judawisastra, 7

L
Latifa Hanum Lalasari, 21;31
Lia Andriyah, 31

M
Mayang Gita Pradisti, 15
Moch Syaiful Anwar, 15

N
Nadia Chrisayu Natasha, 21; 31

S
Septian Adi Candra, 7
Soesaptri Oediyani, 31
Sri Harjanto, 21
Syahwira Taqwa Triadi, 7

T
Tiya Khairina Izzat, 1
Tri Arini, 31

Y
Yorina Sarah, 1
Yosephin Dewayani, 21

SUBJECT INDEX

A
aluminium 2024, 1
austenitic stainless steel 316L, 15

C
coefficient of friction, 1
Cr-Mn austenitic stainless steel, 7
crystal structure, 31

D
DPD (dynamic plastic deformation), 7

E
electrolysis, 31

G
grain growth kinetics, 15

H
Hardness, 15

K
Kekerasan, 17

L
lithium ion separation, 21

M
magnesium ion separation, 21
manganese dioxide, 31
manganese sulfate, 31
modeling, 15

N
nano-twins, 7

P
pin-on-disk test, 1
polymorphy, 31

R
repetitive hammering, 7

S
Seawater, 21
SFE (stacking fault energy), 7
sodium silicate residue, 21

U
uji pin-on-disk, 1

W
wear resistance, 1